THESIS FOR THE DEGREE OF LICENCIATE OF ENGINEERING

Palladium-based Nanoplasmonics for Ultrafast and Deactivation-Resistant Hydrogen Detection

IWAN DARMADI

Department of Physics

CHALMERS UNIVERSITY OF TECHNOLOGY

Gothenburg, Sweden 2019

Palladium-based Nanoplasmonics for Ultrafast and
Deactivation-Resistant Hydrogen Detection
IWAN DARMADI

Department of Physics
Chalmers University of Technology
SE-412 96 Gothenburg
Sweden
Telephone + 46 (0)31-772 1000

Cover illustration:
Hydrogen sensors are indispensable in hydrogen fuel cell cars to guarantee safe operation. A polymer-encapsulated Pd alloy nanodisk hydrogen sensor is illustrated.
(This cover has been designed using creative common license resources from freepik.com.)

Printed at Chalmers Reproservice
Gothenburg, Sweden 2019

Palladium-based Nanoplasmonics for Ultrafast and
Deactivation-Resistant Hydrogen Detection

Iwan Darmadi
Department of Physics
Chalmers University of Technology

Abstract

Hydrogen gas is the energy carrier in the hydrogen economy scenario since energy produced by its reaction with oxygen only leaves water as by-product. However, hydrogen is flammable when mixed with air even at low concentration, *i.e.* above 4 vol.%. Therefore, safety systems are mandatory to monitor and prevent leaks. However, existing hydrogen sensor technology does not meet the stringent future performance targets for safety sensors.

Motivated by this fact, in this thesis I exploit the localized surface plasmon resonance of Pd and Pd-alloy nanoparticles in the quest to develop next generation optical hydrogen sensors. The unique features of an optical sensor are the inherent spark-free operation, the remote readout by light and the possibility for multiplexing. Specifically, I focus on two key aspects related to the hydrogen sensor challenge: (i) the development of Pd-alloy based nanoplasmonic sensors that are both deactivation resistant and meet the stringent response time target, and (ii) the fundamental understanding of nanoparticle-hydrogen interactions in the presence of different coatings.

As the key results, I have developed two different types of plasmonic hydrogen sensor platforms either based on a PdAuCu ternary alloy or utilizing thin polymer film coatings. They exhibit exceptional deactivation resistance towards poisoning gases like carbon monoxide or nitrogen dioxide, and they meet the most stringent sensor response time target defined by the US Department of Energy. Furthermore, I have devised generic design rules for the optimization of plasmonic hydrogen sensor detection limits based on fundamental understanding, and systematically characterized the impact of surfactant molecules widely used in colloidal synthesis of Pd nanocrystals on their interaction with hydrogen gas. All in all, these findings hopefully contribute to a safer hydrogen economy in the future.

Keywords: localized surface plasmon resonance, nanoparticle, plasmonic sensing, hydrogen, palladium, Pd, palladium hydride, palladium alloy, polymer, surfactant, hydrogen sensor.

List of appended papers

This thesis in based on work presented in the following papers:

I. *Rationally-Designed PdAuCu Ternary Alloy Nanoparticles for Intrinsically Deactivation-Resistant Ultrafast Plasmonic Hydrogen Sensing*
Iwan Darmadi*, Ferry A. A. Nugroho*, Shima Kadkhodazadeh, Jakob B. Wagner, and Christoph Langhammer
*equal contributors
Submitted.

II. *Metal-polymer Hybrid Nanomaterials for Plasmonic Ultrafast Hydrogen Detection*
Ferry A. A. Nugroho, Iwan Darmadi, Lucy Cusinato, Arturo Susarrey Arce, Herman Schreuders, Lars Bannenberg, Alice Bastos da Silva Fanta, Shima Kadkhodazadeh, Jakob Wagner, Tomasz Antosiewicz, Anders Hellman, Vladimir Zhdanov, Bernard Dam, and Christoph Langhammer
Nature Materials, published online, 2019. DOI: 10.1038/s41563-019-0325-4

III. *Universal Scaling and Design Rules of Hydrogen-Induced Optical Properties in Pd and Pd-Alloy Nanoparticles*
Ferry A.A. Nugroho, Iwan Darmadi, Vladimir P. Zhdanov, and Christoph Langhammer
ACS Nano, 2018, 12 (10), pp 9903–9912.

IV. *The Impact of Surfactants and Stabilizers on Palladium Nanoparticle Surface Catalyzed Reactions with Hydrogen*
Alicja Stolas*, Iwan Darmadi*, Lucy Cusinato, Ferry A. A. Nugroho, Anders Hellman, Kasper Moth-Poulsen, and Christoph Langhammer
*equal contributors
Submitted.

My contribution to the appended papers

Paper I

I fabricated the samples, did the material characterization (XPS, SEM, UV-visible spectroscopy), carried out the sensing tests, analyzed the data, and wrote the first draft.

Paper II

I fabricated the PMMA and tandem-samples, did the sensing tests and analyzed the data.

Paper III

I fabricated the PdCu samples, did the experiments, and analyzed the data.

Paper IV

I fabricated the samples, did the material characterization (XPS, SEM, UV-visible spectroscopy), carried out the hydrogen sensing experiments, analyzed the data, and wrote the first draft.

Contents

1 Introduction

1.1 Hydrogen Sensors: Today and In The Future

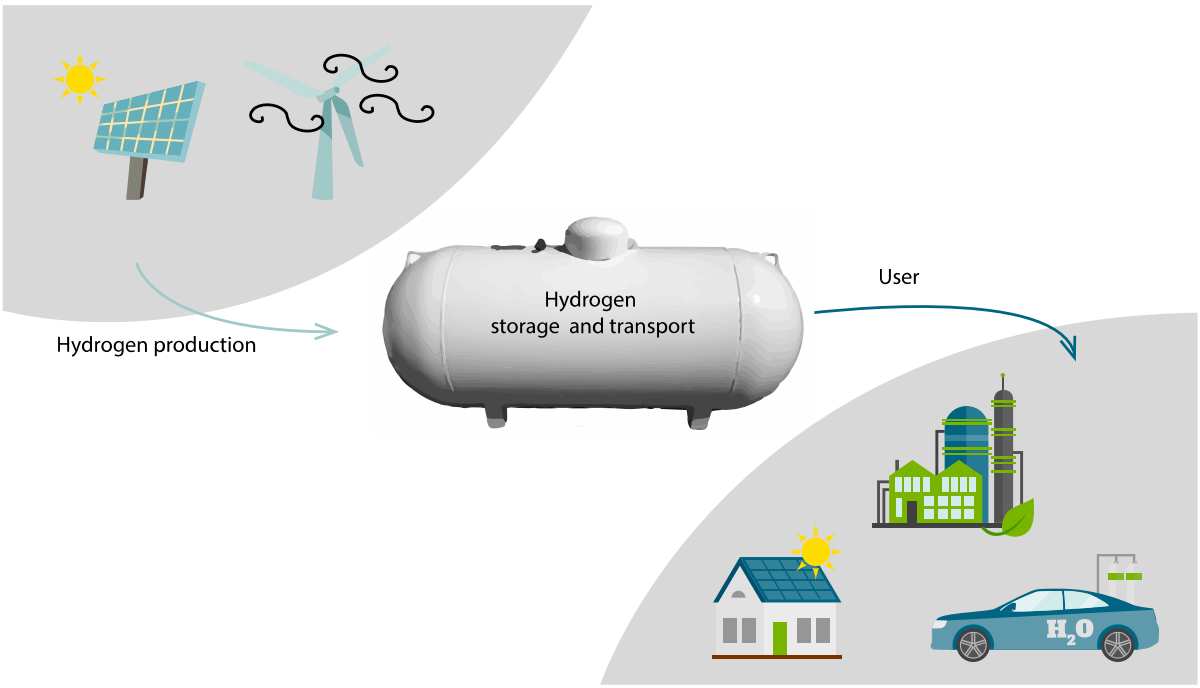

Figure 1: Illustration of the hydrogen economy scenario, in which hydrogen gas plays a central role as a carbon-free energy carrier. Hydrogen can be produced with sustainable energy sources, such as photovoltaic cells or wind turbines. After production, the hydrogen is stored and transported to a wide range of consumers such as industry, buildings, and fuel-cell cars (the illustration was designed using creative commons license resources from freepik.com).

Many may not be aware that hydrogen gas already plays a crucial role in industry today. To be more specific, 90% of the world hydrogen production goes to fine chemical synthesis, crude oil refineries, and metal processing industries[1]. Moreover, all the electronic gadgets that we virtually cannot live without today use semiconductor materials as a basic building

block. Did you know that hydrogen is critical in numerous stages of semiconductor processing, such as annealing, epitaxy, deposition, and stabilizing?[2,3]

To this end, wherever hydrogen gas is used in industrial applications, hydrogen sensors are necessary for at least two reasons: (i) for safety and (ii) for process monitoring. Safety systems are necessary since hydrogen is flammable in ambient air in the range of 4-75 vol-%. Since hydrogen gas is odorless and transparent to light, human senses cannot identify leaks, which makes appropriate sensors very important. For industrial process monitoring, the commercially used hydrogen detectors, such as gas chromatographs, mass-spectrophotometers or specific ionization gas pressure sensors, usually require long sampling time. Additionally, they are very large, expensive and require regular calibration[4]. Therefore, both for established technologies and for the emerging *hydrogen economy*, new hydrogen sensor technologies need to be developed.

The hydrogen economy is a scenario where hydrogen gas is utilized as the main energy carrier[5,6]. Within a fuel cell device, hydrogen and oxygen electrochemically generate electricity and produce water. This should be compared to the traditional fossil fuels, which are converted in CO_2 and other harmful gases, such as CO, NO_x, SO_x, upon combustion. Hydrogen gas, however, does not exist in its molecular form H_2 on earth and requires energy to be produced. Thus, hydrogen is an energy *carrier* (like a battery) and *not* an energy source. In an ideal scenario, hydrogen is produced by electrolysis from water (which is abundant on earth) with sustainable energy resources like wind or solar power[7].

However, despite these prospects, the hydrogen economy is not reality yet since it faces challenges relating to all sub-aspects, that is, hydrogen production, storage, and fuel-cell

development. In fact, most hydrogen produced today is made by steam reforming or partial oxidation of methane[8]. This is, of course, not sustainable and does not fit the hydrogen economy spirit since a fossil energy source is used, because significant amounts of CO_2 are released, and since direct methane combustion itself is more energy efficient than taking the "detour" via hydrogen[9,10].

In spite of these remaining challenges, the day a hydrogen economy is successfully implemented, the demand for hydrogen sensors will increase significantly because leak detection is necessary at every stage from hydrogen production, to transportation, to the end-usage[11]. Furthermore, the applications of hydrogen sensors are not only limited to the industry and the hydrogen economy. There are potential applications of hydrogen sensors in other fields, which are equally interesting, for example disease diagnosis and industrial infrastructure malfunction inspection. *Table 1* lists applications of hydrogen sensors today both at the lab and industrial scale.

Table 1 Applications of hydrogen sensors today

Application	Role of hydrogen sensor	Ref.
Energy		
1. Hydrogen fuel cell.	Leak detection and monitoring.	12,13
Industries		
1. Ammonia and methanol synthesis.	Hydrogen precursor monitoring.	4,14
2. Hydration of hydrocarbons.		15
3. Desulphurization of petroleum products.		15
4. Rocket fuel production.		15
5. Semiconductor industries.		2,3
Probing		

1. Nuclear power plants.	Leak detection in waste tanks. Hydrogen forms during plutonium radiolysis.	[16,17]
2. Transformer failure detection.	Hydrogen is dissolved in transformer oil when there is malfunction.	[18–20]
3. Coal mines.	Hydrogen is an early fire indication since it is formed in ppm range by methane and coal.	[15,21,22]
4. Lighting industry.	Hydrogen is a contaminant to be avoided in the xenon, neon and krypton lighting industries. Sensor is needed to monitor the contamination level.	[15]
Biomedical and food science		
1. Intestinal disease detection.	For certain conditions, lactose, glucose, and fructose are not absorbed perfectly by the intestine. Bacteria digest these molecules to produce hydrogen. Breath test to detect hydrogen. Typical hydrogen concentration is 10-20 ppm.	[23]
	In vivo study of H. pylori (peptic ulcer pathogen) in mouse stomach mucus. H_2 sensor corelates H_2 production with bacteria number.	[24]
	others	[25–28]
2. Hydrogen for disease therapy.	Monitoring of hydrogen absorption by tissue.	[29,30]
3. Bone implant inspection.	Mg alloy biodegradation generates hydrogen gas.	[31,32]
4. Irradiated frozen food quality control.	Hydrogen is produced *via* radiolysis during irradiation. The hydrogen concentration decreases overtime and can be used as marker of the irradiated-food aging.	[33,34]

1.2 Hydrogen Sensing Technologies

There is a wide range of hydrogen sensing technologies in R&D and at the commercial stage.

Hubert *et al*. list eight types of hydrogen sensing principles/technologies[4,15]:

- Catalytic
- Thermal conductivity
- Electrochemical
- Resistance based
- Semiconductor work function based
- Mechanical
- Acoustic
- Optical

A catalytic sensor works by combusting hydrogen and oxygen on a catalyst surface. The combustion releases heat that induces a change in electric resistance. The most commonly used catalyst is platinum. Catalytic-type sensors, however, detect *any* combustible gas other than hydrogen also, which makes selectivity an issue. To enable the sensor to operate, at least 5-10% oxygen is required[15].

A thermal conductivity type sensor operates based on a heat transfer rate difference of gases. For instance, hydrogen's thermal conductivity is 0.174 W/mK, while air has a thermal conductivity of 0.026 W/mK at room temperature[4]. The basic construction of this sensor consists of two resistors separated at a certain distance. One resistor is heated, while the other is used to measure heat transfer from the first resistor. Since there is no active catalytic element involved, this sensor is inherently more stable and not sensitive to poisoning. However, high thermal conductivity gases such as He, Ar, and CO may interfere with hydrogen readout[35].

An electrochemical sensor detects hydrogen from the electrochemical reaction of the electrode with hydrogen ions[36]. This type of sensor deploys an electrochemical cell construction, where two electrodes are separated by either a liquid or solid electrolyte. H_2 is absorbed by the electrolyte (e.g. sulphuric acid) and dissociates into H+ ions. Then, the contact with the electrode leads to a potential change across the cell. Since

most cells utilize a platinum electrode, electrochemical sensors are usually impaired by CO poisoning.

A resistance-based sensor employs the resistivity change of a metal oxide or metal upon exposure to a reducing gas. Typical semiconducting metal oxides used in this type of sensors are SnO_2, ZnO, WO_3, FeO[15,37]. There are several different mechanisms behind metal oxide sensors. One of those is the reaction of hydrogen with adsorbed oxygen, which changes the metal oxide resistivity. A metallic resistive sensor works along a different mechanism. Some metals like Pd or Mg form metal-hydrides in the presence of hydrogen. The metal-hydride phase then typically exhibits higher resistivity compared to the metallic counterpart. The shortcomings of metal oxide sensors are poor selectivity and the requirement of oxygen for operation. Metallic resistance sensors usually suffer from CO and sulfuric compound poisoning due to employment of Pd as active or capping element, which is required for H_2 dissociation.

A semiconductor work function-based hydrogen sensor consists of metal, oxide, and semiconductor (MOS) layers. The work function is the energy required to remove an electron from a solid to vacuum. The oxide is usually coated with Pd to dissociate hydrogen molecules, which later spills over into the oxide bulk. The spillover consequently raises polarity at the oxide-semiconductor interface that shifts the semiconductor work function.

A mechanical sensor exploits structural changes of a hydrogen-absorbing material upon hydrogen detection. The simplest example of a mechanical sensor is a Pd

cantilever sensor, which measures the Pd volume expansion during hydrogen absorption, and vice versa during desorption[38]. However, due to the Pd-hydride expansion-contraction cycles, mechanical sensors have typically quite poor long-term mechanical stability. Other example for a mechanical sensor is based on discontinuous Pd nanostructures[39–41].

An acoustic gas sensor exploits a material's acoustic wave sensitivity towards hydrogen adsorption or absorption. An example of such a sensor is the quartz crystal microbalance (QCM). The quartz crystal is a piezoelectric material, i.e. material that deforms under an external electric field. For molecular detection, an external wave generator is used to induce the oscillation of the quartz crystal at its resonance condition. For hydrogen detection, the crystal is typically coated with a Pd layer, which absorbs hydrogen and forms a hydride. The crystal resonance is then very sensitive to the hydrogen absorption/desorption in the Pd layer on its surface and changes in the resonance frequency of the crystal are used as readout[42,43]. Other examples of acoustic hydrogen sensors are surface acoustic wave sensors[44] and sound velocity measurements[15].

An optical sensor exploits material optical property alterations upon hydrogen detection. Pd is utilized mainly also in this type of sensor due to the optical contrast between Pd and Pd-hydride and due to the barrierless and reasonably fast hydrogen absorption[45]. Other hydrides such as Hf-, Y-, Mg-, Ta-, V-hydride offer larger optical contrast but suffer from (very) slow response and still need a Pd capping layer[46–51]. Another active material for optical sensors is WO_3 since it exhibits a color change upon hydrogen adsorption. There are many modes to read optical sensors e.g.

transmission, reflectance, frequency, polarization, and phase shift. Optical sensors have advantages compared to other sensor technologies since they inherently have no risk of spark generation, are unaffected by electromagnetic interference, are possible to multiplex, have a wide dynamic range, and do not require oxygen for operation[4]. Eye-readable optical hydrogen sensors have also been developed, which provides opportunities for low-cost mass production since extra costs generated by light sources and detectors can be eliminated[48,52,53].

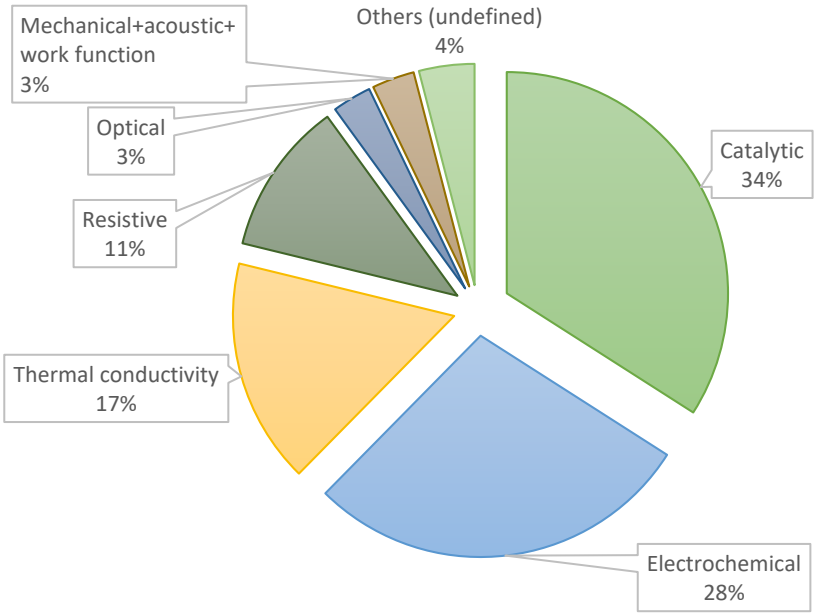

Figure 2: Hydrogen sensor technology distribution chart from 2015 listing 420 different hydrogen sensors available on the market[54].

Based on the 2015 H2sense hydrogen sensor database that listed 420 different sensors on the market, catalytic-type sensors dominate hydrogen sensor technology today, followed by electrochemical-type sensors, of which most users are in the chemical processing industries[54]. The reason behind the catalytic-type sensor's popularity is probably its simple construction, despite its high operational power consumption and high cross-sensitivity to combustible gases. The electrochemical sensors' construction is also relatively simple, while it exhibits

excellent hydrogen sensitivity and requires a low amount of power to operate. The sensor sensitivity, however, degrades quickly over time due to electrode erosion. The shortcomings of electrochemical sensors are slow response/recovery time and high cross-sensitivity towards CO, Cl_2, SO_2, H_2S, and NO_x[4,36].

1.3 Challenges of Hydrogen Sensors

Requirements for hydrogen sensors depend on the specific application. For instance, in a safety system, response time is much more prioritized than wide dynamic range. On the other hand, for process monitoring application, dynamic range may be more important than fast response time. For the safety system application there are different requirements for an automotive and a stationary system[4]. There are several hydrogen sensor requirement standards but the most stringent one was released by the US DOE (Department of Energy) in accordance with automobile manufacturers' demands in 2015[4]. The stationary system requirements are less strict[4].

Table 2: Technical requirements for hydrogen safety sensors for automotive and stationary applications[4].

Parameter	Automotive	Stationary
• Measurement range	Up to 4 v%	Up to 4 v%
• Detection limit	< 0.1 vol.%	< 0.1 vol.%
• Response time	< 1 s	< 30 s
• Recovery time	< 1 s	< 30 s
• Ambient temperature	- 40 to +85˚C	- 50 to +50˚C
• Ambient pressure	62-107 kPa	80-110 kPa
• Ambient humidity	0-95%	20-80%
• Power consumption	< 1 W	-
• Lifetime	6000 h	3-5 years
• Overall accuracy	± 5% of reading	±10%

Pd plays a central role in most hydrogen sensor technologies. Therefore, technical requirements presented in *Table 2* that are not met are usually the consequence of inherent Pd shortcomings[55], such as:

- Poisoning by CO or sulfuric compounds (leads to poor sensor lifetime and low accuracy).
- Hydride hysteresis (leads to low sensor accuracy).
- Mechanical instability due to Pd-hydride lattice expansion by approximately 10% (leads to poor sensor lifetime and stability).
- Hydrogen diffusion/recombination-limited rate (leads to slow response/recovery time).

It is worth noting, however, that a complete sensor *system* consists of the active element (e.g. Pd) and the supporting systems (e.g. light source, detector, electrolyte, electrode, etc.). Thus, the sensor system's performance is not only dictated by limitations of Pd as active element.

1.4 State of The Art of Hydrogen Sensors

It is very difficult to find scientific reports about hydrogen sensors that address all aspects of the technical performance requirements. In case it exists, the listed sensors don't fulfill all points of the requirements in *Table 2*. For example, some sensors are excellent with respect to response time but poor with respect to other aspects, such as high operational temperature or exhibit hysteresis in their signal[55]. As part of our own analysis of this field, we have listed 49 of the fastest hydrogen sensors published in peer-review scientific journals in *Table 3*. Out of fast-response sensors, around 80% are electrical, which contrasts commercially available sensors that are mainly catalytic and electrochemistry-based. Furthermore, roughly 90% of the reported sensors utilized Pd as capping/active element, which clearly implies that their

performance is limited by the inherent Pd shortcomings mentioned in the previous subsection.

From the 49 reports, only 3 sensors fulfill the stringent target of a response time < 1 s at hydrogen pressure around 4 vol.-%, and none has yet achieved a response time < 1 s at 0.1 vol.-% as demanded by the DOE target for automotive applications[56]. However, there are sensors, which have been close to the DOE target. One reported 0.07 s response time at 4 vol.-% H_2 for a resistive Pd-mesowire sensor[57], while another work also achieved 0.07 s response time at 2 vol.-% H_2 using resistive ultrathin Pd nanogaps[58]. Unfortunately, the recovery time was not specified in these reports. Another report claimed 0.5/0.5 s response/recovery time for a resistive PdNi nanogap sensor operated at room temperature[40]. The reported detection limit in ref.[40] is 500 ppm ,which is quite impressive (less than 0.1 vol.-% as required in *Table 2*). The choice of PdNi is interesting since its response towards 1-4 vol.-% hydrogen is more linear than for the traditional Pd solution. An additional notable fact is that all response/recovery sensors mentioned above were achieved by reducing the material size to the nanoscale since the surface/volume ratio of nanosized materials is (much) larger than for bulk materials or thin films. In this way, the typically diffusion rate limited hydrogen absorption time is dramatically reduced. When it comes to the detection limit, in the majority (ca. 70%) of reports it is somewhat below or equal to 1000 ppm (< 0.1 vol.-%).

However, two other critical characteristics are not addressed in almost any of the scientific reports on hydrogen sensors: the hysteresis aspect and cross-sensitivity/poisoning. In fact, there are only four reports that discuss the hysteresis problem: PdAu films and particles[59–61], and PdCuSi-film[62,63]; all of them are reported to be hysteresis free. Cross-sensitivity means that the sensor is responsive to the presence of another gases than hydrogen. Poisoning, on

the other hand, refers to deactivation of the sensor when exposed to a certain gas. In the case of poisoning, CO, NO_x, and sulfuric compounds have been well known to deactivate Pd, not only in Pd-based hydrogen sensors but also in separation membrane and catalyst technology[64–69]. In contrast to cross-sensitivity, the poisoning effect is often retained even when the poisoning species is no longer present in the gas, since it is strongly bonded to the Pd surface. To this end, only 37% of the reports in *Table 3* (page 14) have investigated cross-sensitivity of the sensor towards various gases, such as O_2[70,71], CO[57,72–79], NO_x[76,79,80], NH_3[78,81], H_2O[70], sulfuric compounds[74,78], hydrocarbons[77,81]. Interestingly, in the case of cross-sensitivity to CO, there are claims of both excellent[76,77,80,82–84] and poor selectivity[74,78,79] for Pd-based sensors. Furthermore, it is frequently reported that Pd sensors are cross-sensitive to ammonia (NH_3)[74,77,78,84]. For the CO poisoning case, to the best of my knowledge there are only four works that investigated the CO poisoning effect on Pd-based hydrogen sensors: Pd mesowires by Favier *et al.*[57,85], PMMA-coated Pd nanoparticles by Chen *et al.*[83] and Hong *et al.*[82] Those works consistently show that CO poisons *bare* Pd sensors.

To finalize this overview of hydrogen sensor technologies, I summarize the hydrogen sensor state of the art as follows. No one has achieved a response time below 1 s at 0.1 vol.-% hydrogen concentration, as set as a target in the DoE standard for automotive applications. Most sensors exhibit limits of detection below 1000 ppm down to 10 ppb[86], which implies that the limit of detection is not a main concern for most applications. Another key observation is that most reports do not comment on the hysteresis problem when Pd is used as active material. Finally, there are many reports that include cross-sensitivity tests but only a very small number of studies have investigated poisoning and deactivation effects, despite their importance for long-term stable operation.

1.5 Aim and Objectives of This Work

The main aims of my project, which have guided all the undertaken research efforts, are:

(i) to study hydrogen and Pd (-alloy) nanoparticle interaction for the purpose of plasmonic hydrogen sensing.

(ii) to develop Pd-based plasmonic nanoparticles that achieve fast response/recovery times towards meeting the stringent DOE target, that are hysteresis-free, and that are resistant to CO-poisoning and deactivation.

Furthermore, the more specific objectives to achieve the aims have been:

(i) to study hydrogen absorption and optical signal correlation of Pd – coinage metal alloy nanoparticles using combined localized surface plasmon resonance (LSPR) and quartz crystal microbalance (QCM) techniques.

(ii) to develop a PdAuCu ternary alloy for fast response, hysteresis-free, and CO-poisoning resistant plasmonic hydrogen sensing.

(iii) to develop PdAu alloy nanoparticle – polymer membrane nanocomposites for fast response, hysteresis-free, and CO-poisoning resistant hydrogen detection.

(iv) to study the effect of surfactants and stabilizers used in colloidal synthesis on hydrogen-Pd nanoparticle interaction kinetics.

Table 3 The state of the art fast response hydrogen sensor obtained from peer-reviewed scientific journals (the list is sorted according to the response time)[87].

No	Active Element	Method†	Response Time (s)‡	Recovery Time (s)ɬ	Pressure (mbar)	Temp. (˚C)	Limit of Detection (ppm)	Measured in	Hysteresis-Free	Poisoning (*P*)/cross-sensitivity (*CS*) test§	Commentary	Ref.
1	Fractured Pd nanowire	E	0.07	-	40	25	10000	Air	no mention	CH_4, CO, H_2O (*CS and P*).	Sensor survived from 3000 ppm CO test with air background.	57
2	Pd nanoparticle/ nanogap	E	0.07	-	20	RT	25	N_2	no mention	none		58
3	PdNi nanogap	E	0.5	0.5	20	RT	500	N_2	no mention	none		40
4	Pd/Mg thin film	E	1	60	4000	100	-	vacuum	no	none		88
5	PdAu nanodisk	O	1		40	RT	-	vacuum	hysteresis-free	none		60
6	Pd@Pt nanowire	E	2	2.5	40	103	4000	Air	no mention	none		89
7	Au/SiO2/Pd film on fiber	O	3	10	40	RT	5000	Ar	no mention	none		90
8	α-MoO3 nanowire	E	3	2.7	15	260	100	Air	no mention	C_2H_5OH, CO, CH_4 (*CS*)	High signal interference (20%) by alcohol.	73
9	Pd nanowire	E	4	-	24	RT	27	N_2	no mention	O_2 (*P*)	O_2 has effect when H_2 test, indication of catalytic activity	71

										on the Pd surface.	
10	Pt/Pd bimetallic film	E	4	5	10	150	10	Air	no mention	N_2, CO_2, CO, NO_2, O_2 (*CS*)	CO leads to more than 10% signal deviation.	[79]
11	UV-activated ZnO nano-network	E	4	24	10	RT	5	vacuum	no mention	none		[91]
12	(La, Sr)(Cr, Fe)$O_{3-\delta}$ Perovskite	E	4	24	1	450	20	N_2	no mention	CH_4, C_3H_8, CO, NO_2, and NH_3 (*CS*)	CO, NO_2 makes more than 10% signal deviation.	[75]
13	Pd on SiC nanocauliflo wer	E	4	48	0.5	300	2	Air	no mention	CO, H_2S, NH_3 (*CS*)	More than 10% signal deviation by the all three gases.	[74]
14	Pd nanoribbon	E	4	> 9	100	RT	20000	Air	no mention	CO_2 (*CS*)		[92]
15	Pd-Au layers on fiber	O	4.5	13	40	RT	-	N_2	no mention	none		[93]
16	Pd nanogap	E	5	200	40	RT	5000	N_2	no mention	none		[41]
17	Pd/Pt on ZnO nanorods	E	5	76	10	100	0.2	Air	no mention	none		[94]
18	PdCuSi alloy MEMS	M	5		30			N_2	hysteresis-free	CH_4, CO_2, He (*CS*)	Excellent selectivity.	[62,63]
19	Pd-Y thin film	O	6	8	40	RT	1000	N_2	no mention	none		[95]

20	Pd-capped Mg thin film	E	6	33	10	RT	1	Air	no mention	NO_2, CO, CO_2, NO_2, O_2 (*CS*)	Excellent selectivity.	[76]
21	Pt-TiO2 nanocomposite	E	10	20	1	RT	30	N_2	no mention	none		[96]
22	Pd-decorated tubular TiO_2	E	12	5	1	180	1	Air	no mention	CO, CO_2, ethanol, acetone, H_2O (*CS*)	Excellent selectivity.	[77]
23	Pd ultra small grain	E	12	19	30	RT	2.5	Air	hysteresis-free	NO_2, SO_2, CO_2 (*CS*)	Excellent selectivity.	[97]
24	Pd nanowire@ZIF 8	E	13	6	1	RT	1000	Air	no mention	none		[98]
25	MoS_2 flakes	E	14	140	10	30	-	Air	no mention	none		[99]
26	Pd@Au nanoparticle	E	15	18	200	RT	1000	N_2	no mention	none		[100]
27	SiO_2 nanorod@Pd	E	17	-	10	RT	10	Air	no mention	none		[101]
28	Pd/Ni film	E	20	100	40	22	-	Air	no mention	none		[102]
29	Pd strip on 3D strtuctures	O	20	-	1	RT	10	N_2	no mention	none		[103]

30	Pd layer on polyurethane fibers	E	24	-	1	RT	20	N_2	no mention	none		104
31	CeO_2-loaded In_2O_3 hollow spheres	E	24.5	21	0.05	160	10 ppb	Air	no mention	none	Excellent LOD	86
32	Pd nanowire	E	25	-	1	RT	50	Air	no mention	none		105
33	Pd nanocube+ TiO_2 nanofiber composite	E	25	1	6	150	6000	Air	no mention	ethanol, nitrogen dioxide and isopropyl alcohol (*CS*).	Excellent selectivity.	80
34	Pd-SnO_2/MoS_2	E	26	15	1	RT	30	Air	no mention	CH_4, C_2H_6, C_3H_8, CO, NH_3 (*CS*)	NH_3 leads to 12% signal deviation.	72
35	Pd decorated MnO_2 nanowalls	E	30	40	1	100	10	Air	no mention	H_2S, NH_3, CO (*CS*)	All gases interfere the signal by more than 10% deviation.	78
36	PdAu nanodisk on fiber optic	O	40	87	40	RT		Air	hysteresis-free	none		61
37	Pd nanoparticle on C-nanowire	E	45	5	1	RT	10	N_2	no mention	none		106
38	TiO_2 nanostructure	E	50	40	1	RT	1	Air	no mention	none		107

39	Pd/ZnO nanowire	E	50		0.1	100	100	Air	no mention	none		[108]
40	Pd microcantilever	M	90	300	10	RT	-	Air	no mention	O_2, H_2O (*CS*)	H_2O interferes the signal.	[70]
41	Pd nanoparticle @ZnO nanorod	E	100	-	5	RT	10	Air	no mention	none		[109]
42	Pt nanowire	E	100	-	1	25	1	Air	no mention	none		[110]
43	Pd nanoparticle +PMMA on graphene	E	108	330	20	RT	250	Air	no mention	CH_4, CO, NO_2 (*CS*)	Excellent selectivity.	[82]
44	Pd doped TiO_2 nanotube	E	120	90	10	RT	-	Air	no mention	CH_4, NH_3, CO_2 (*CS*)	NH_3 leads to more than 10% signal deviation.	[81]
45	Pd–Ag Composite Nanowires	E	120	102	1	RT	100	Air	no mention	no		[111]
46	Pd/Pt coreshell on graphene	E	180	72	10	RT	1	Air	no mention	none		[112]
47	MoS_2 nanoparticle on graphene	E	251	260	0.5	60	200	vacuum	no mention	NH_3, NO (*CS*)	More than 10% signal deviation by the all two gases.	[84]
48	Pd NP@graphene	E	300		1	22	20	N_2	no mention	none		[113]

49	Pd nanogap	E	498	300	30	RT	20000	N_2	no mention	none	[114]

† Detection method: Electrical (E), mechanical (M), optical (O).

‡Response time is defined as t90, the time required to reach 90% of the saturated signal.

⸸Recovery time is defined as t10, the time required to reach 10% of the saturated signal.

§Cross-sensitivity (CS) test refers to response test when the sensor is exposed to gas other than hydrogen. Poisoning (P) test refers to response test when the sensor is exposed to hydrogen and a test gas mixture.

2 Theory Overview

In this chapter, I will discuss the following topics:

- **Localized surface plasmon resonance**: the principle of nanoscale plasmonic sensing I exploit to detect hydrogen by using nanosized Pd and its alloys.
- **Thermodynamics of Pd - coinage metal alloys**: the mixing of Pd with other noble metals, i.e. Au and Cu, at the atomic level. Pd alloys are of interest in my project to alleviate inherent Pd shortcomings in hydrogen sensor applications, i.e. hysteresis, CO-poisoning and slow response.
- **Thermodynamics of Pd (alloy) hydrides**: the interaction between hydrogen and Pd (alloys) to form hydride compounds. Pd hydride has different optical properties compared to Pd, which gives rise to a measurable optical contrast between the two states that is exploited for sensing.

2.1 Localized Surface Plasmon Resonance

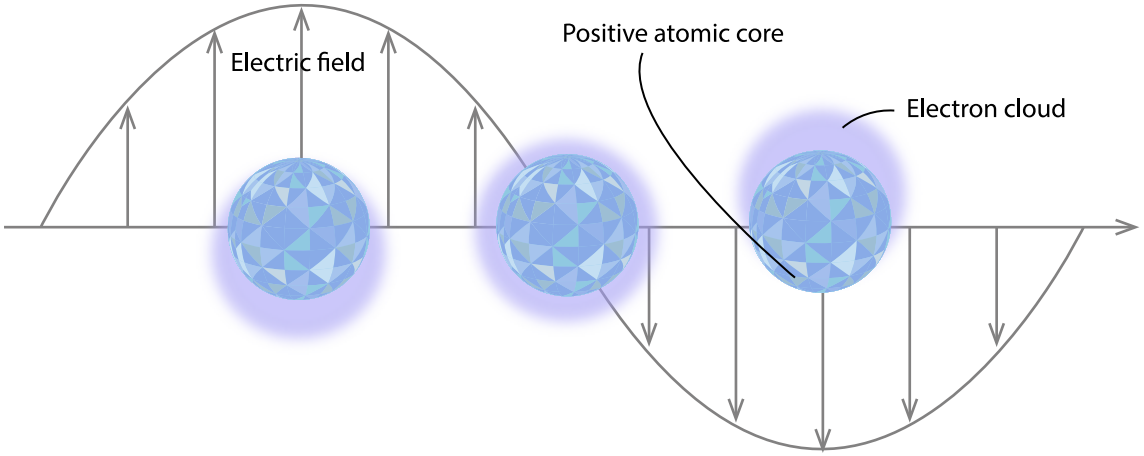

Figure 3: Localized surface plasmon resonance (LSPR) of a metallic nanoparticle. At the resonance condition, the nanoparticle's free electrons are driven by the electromagnetic field of an incoming plane light wave.

Localized surface plasmon resonance (LSPR) is a collective electron oscillation of metallic nanoparticles driven by an electromagnetic wave, i.e. light (*Figure 3*). The nanoparticle and light interaction can be explained in the so-called quasi-static approximation, where the nanoparticle size is assumed to be much smaller than the wavelength of the incoming light ($d \ll \lambda$). The interaction leads to light absorption (σ_{abs}) and scattering (σ_{sca}), which in sum is called extinction (σ_{ext}). For the special case of a sphere, they can be expressed analytically in term of cross-section (σ) as follows[115]:

$$\sigma_{ext} = \frac{18\pi\varepsilon_m^{3/2}V}{\lambda}\frac{\varepsilon_2(\lambda)}{[\varepsilon_1(\lambda)+2\varepsilon_m)]^2+\varepsilon_2(\lambda)^2} \quad \textit{eq. 1}$$

$$\sigma_{sca} = \frac{32\pi^4\varepsilon_m^2V^2}{\lambda^4}\frac{(\varepsilon_1-\varepsilon_m)^2+\varepsilon_2(\lambda)^2}{[\varepsilon_1(\lambda)+2\varepsilon_m)]^2+\varepsilon_2(\lambda)^2} \quad \textit{eq. 2}$$

$$\sigma_{abs} = \sigma_{ext} - \sigma_{sca} \quad \textit{eq. 3}$$

Where λ is the light wavelength and V is the nanoparticle volume. ε_1 and ε_2 denote real and imaginary parts of the nanoparticle dielectric function, respectively. ε_m denotes the real part of the nanoparticle's surrounding medium dielectric function. A resonance condition occurs when the cross-section is maximal, which is achieved by minimizing the denominator, i.e. when $\varepsilon_1 = -2\varepsilon_m$. From a practical perspective, the resonance appears as a peak in the extinction or absorption spectrum. From the expressions above one can also see that the interaction clearly depends on the nanoparticle material itself and on the surrounding medium. Furthermore, beyond the approximation above, nanoparticle-light interaction also depends on the nanoparticle shape and arrangement in an array via far-field interactions[116].

In the visible light region, Au and Ag nanoparticles have a small dielectric function imaginary part (ε_2), which means that they scatter light efficiently[117]. This is why they are widely used as plasmonic materials. Other metals, e.g. Pt, Pd, Cu, Al[118], are less attractive since they have larger ε_2, which dampens the plasmonic resonance via interband transitions.

2.1.1 Plasmonic Sensing

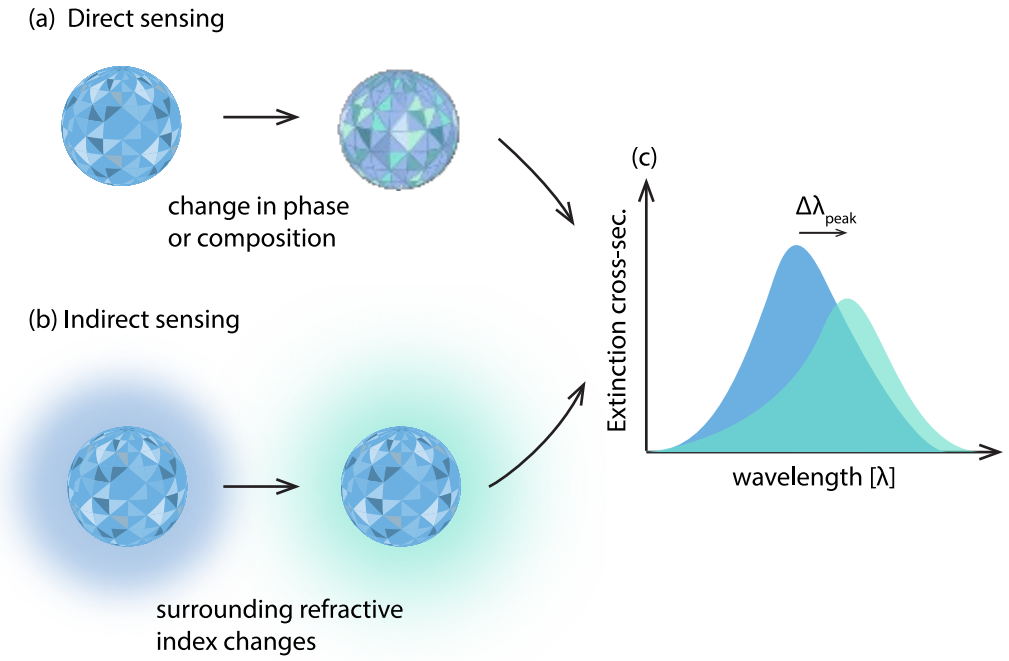

Figure 4: Two different ways of plasmonic sensing: (a) direct sensing, where the phase or compositions of the plasmonic nanoparticle changes and (b) indirect sensing, where the nanoparticle itself is inert but the medium around it (i.e. the refractive index) changes. Both mechanisms lead to LSPR shifts, as depicted in (c).

Since the interaction with light depends on the nanoparticle and the surrounding medium, one can use it to "probe" nanoscale phenomena. This is the concept of plasmonic sensing. *Direct sensing* refers to sensing due to a change within the nanoparticle itself (e.g. phase transformation or composition change), while *indirect sensing* refers to sensing due to a change of the surrounding medium[119,120] (*Figure 4*). Direct sensing is the fundamental principle in this thesis, where we exploit the hydride formation in Pd and its alloys to detect hydrogen gas. This is possible due to the distinct optical permittivity contrast between Pd and Pd hydride[121,122].

For indirect sensing, the dependence of the plasmonic resonance on the surrounding medium refractive index can be derived from the Drude model[115]:

$$\lambda_{max} = \lambda_p \sqrt{2n_m^2 + 1} \qquad \textit{eq. 4}$$

where λ_{max} is the LSPR frequency and λ_p is the bulk plasma frequency. n_m denotes the refractive index of the surrounding medium. Based on this principle, there are plasmonic sensors for a wide area of applications, including biosensors[123–125], gas sensors[126–128] and spectroscopy [129,130].

2.2 Thermodynamics of Pd (Alloy) Hydrides

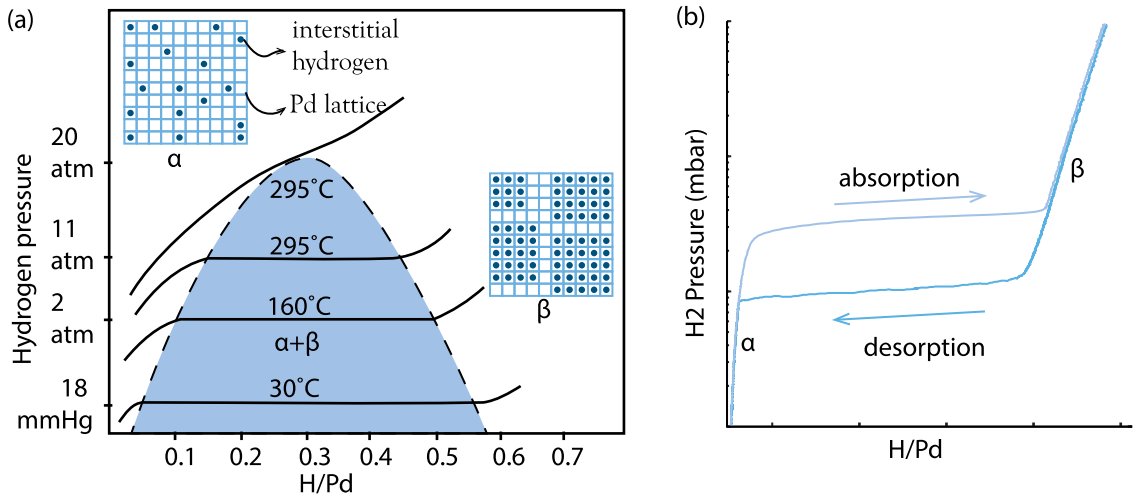

Figure 5: Pressure-composition isotherms of Pd hydride and the corresponding phase diagram. (a) At low hydrogen pressure, interstitial hydrogen is sparsely distributed in the Pd lattice (α-phase). At high hydrogen pressure, the hydride forms (β-phase). Below a critical temperature Tc, a plateau region exists and denotes the co-existence of α- and β -phase. Above the Tc, the plateau disappears and thus α and β-phases are not distinguishable anymore and the phase-transformation is no longer first-order (the figure is adapted from [131]*). (b) Hysteresis: the absorption and desorption processes follow different paths in the pressure-composition isotherm.*

Pd-hydride is one of the simplest metal-hydride systems and has therefore been studied for a long time as *the* model for such materials. When the diatomic hydrogen molecule adsorbs on a Pd surface, it dissociates into two hydrogen atoms essentially without activation barrier. From the surface, these atoms diffuse first into subsurface interstitial sites (which is the rate limiting step) and then into bulk interstitials in the Pd, forming Pd-hydride once a high enough concentration has been reached (Pd-H_x). Corresponding hydrogen absorption isotherms are shown in *Figure 5a.* At low hydrogen pressure, the interstitial hydrogen atoms

are sparsely distributed in the Pd lattice in a solid solution called the α-phase. In this regime, Sieverts' law applies: *the content of diluted hydrogen is proportional to square root of applied hydrogen (partial) pressure.* At a critical pressure, attractive H-H interactions mediated by lattice strain induce the nucleation of the hydride or β-phase, as indicated by the onset of the plateau in the isotherm. At room temperature, the maximum hydrogen solubility (expressed as H/Pd) in bulk Pd in the α- and β-phase at room temperature are 0.017 and 0.65, respectively[42,132]. For bulk Pd, the equilibrium plateau, across which the α- and β-phase co-exist, occurs at a pressure around 24 mbar at 30˚C[131].

From isotherms measured at different temperature, one can derive the phase diagram for the Pd – hydrogen system (dashed-line in *Figure 5*). As temperature is increased, the plateau elevates to higher pressure and the width of the two-phase coexistence region becomes narrower, until it vanishes at the critical temperature (Tc). At T ≥ Tc, α- and β-phase are not distinguishable anymore and the phase transformation is no longer of first order. For bulk Pd, Tc is in the range of 290 ˚C[131,132].

Hydrogen absorption into Pd has also structural implications. Pd has a face-centered-cubic (fcc) crystal structure with lattice constant 3.887 Å. In the α-phase, the lattice constant increases up to 3.895 Å, before it more dramatically increases to 4.025 Å in the β-phase[132]. Thus, upon hydride formation, the lattice volume grows by approximately 10%. The volume expansion consequently makes Pd prone to structural degradation (e.g. cracking and peeling) after cycle(s) of hydrogen (de)absorption, which is a problematic issue in applications like separation membranes and hydrogen sensors. This issue can be alleviated by several strategies, such as reducing the Pd size to smaller dimensions down to the nanometer scale, by alloying the Pd with other metals (e.g. Au, Ag, Cu[133–135]), or by using a proper support[135,136]. It is also worth noting, however, that the volume expansion is not always a

shortcoming for applications since, for instance, mechanical hydrogen sensors rely on this effect[38,39].

The relation between pressure and the hydrogen-metal ratio (H/M) depends on the pressure direction, i.e. increasing/absorption or decreasing/desorption, as presented in *Figure 5b*, due to the inherent hysteresis of the Pd-H system. Specifically, experiments have shown that the plateau pressure of the absorption branch is always higher than the one of the desorption branch. In brief, this can be explained by the fact that the hysteresis gap is the consequence of an energy difference between the relaxed metallic Pd lattice and the expanded Pd hydride lattice due to lattice strain. This creates an energy barrier that has to be overcome before the hydride is formed, which effectively means that a higher/lower hydrogen pressure has to be applied for the hydride to form/decompose, compared to a strain-free ideal system[137].

For sensor applications, hysteresis leads to ambiguous readout. However, the hysteresis problem can be mitigated by either increasing the operational temperature above the Tc (above which hysteresis disappears) or by alloying with other metals[55]. To this end, several Pd alloys have been reported as hysteresis-free at room temperature, for instance PdAu[59–61,138], PdNi[139], and PdCuSi[63].

2.2.1 Pd Alloy Hydrides

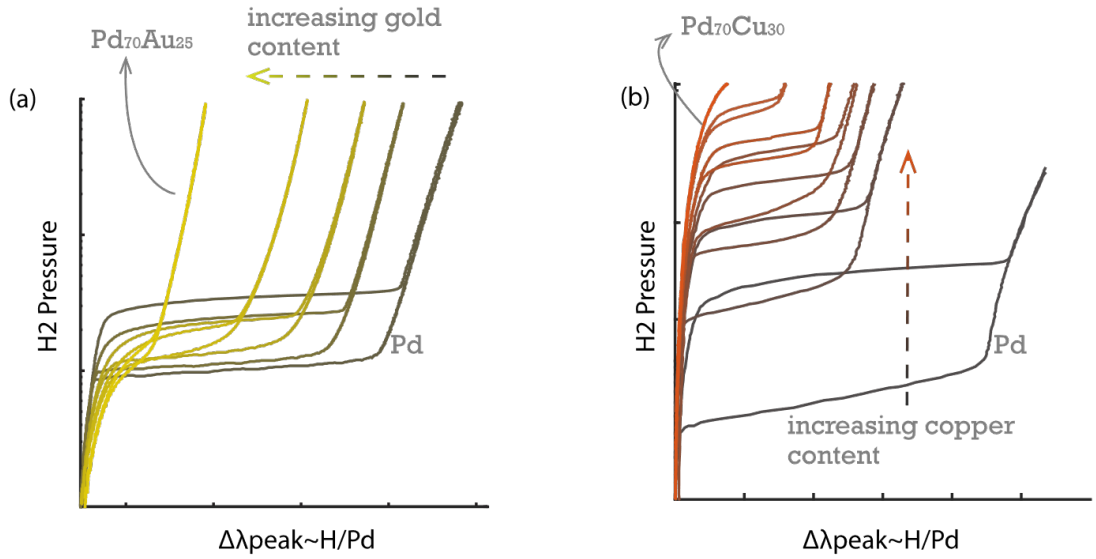

Figure 6: Pressure-LSPR peak shift isotherms of (a) PdAu and (b) PdCu alloy nanoparticles obtained at 30˚C and in the 1-1000 mbar hydrogen pressure range. For PdAu, increasing Au content reduces hysteresis width. At 25 at.% Au, the isotherm is hysteresis-free. For PdCu, increasing Cu content reduces hysteresis width and elevates de/absorption plateau pressures simultaneously. At 30 at.% Cu, only the α-phase exists even at 1 bar H_2.

For sensor applications, Pd possesses several major drawbacks. One of the drawbacks is the presence of hysteresis, which can be mitigated by alloying. In my work, three Pd alloys were of interest, namely binary PdAu and PdCu, and the ternary system PdAuCu.

The hydrogen sorption isotherms for these alloy systems are different to those of Pd and depend strongly on the alloyant concentration. For example, in the PdAu binary system, the hysteresis gap tends to be narrower (i.e. absorption plateau pressure drops while desorption plateau pressure raises) with increasing Au concentration (*Figure 6a*). This, in brief, is the consequence of the Au atomic radius being larger than that of Pd. Hence, it induces lattice

expansion to the Pd host, which consequently reduces the energy barrier (pressure) to transform from the α to the β phase. On the other hand, the PdCu binary system behaves differently compared to PdAu (*Figure 6b*). As the Cu content is increased, both absorption and desorption plateaus elevate to higher pressure and, at the same time, the hysteresis gap shrinks. In contrast to Au, the atomic radius of Cu is smaller than that of Pd and its presence contracts the Pd host lattice. At 30 at.-% Cu, only the α-phase exists within the 1-1000 mbar hydrogen pressure range. These trends that I have obtained from my nanoparticle samples are consistent with previous studies of PdAu[59,60] and PdCu[63,140,141] thin film/bulk systems. To this end, in **Paper III,** we have also shown that the hydrogen - Pd ratio in these alloys scales linearly with the optical plasmonic response[42].

2.3 Thermodynamics of Pd-Coinage Metal Alloys

In this subsection I discuss the thermodynamics of palladium-coinage metal alloys. Stability of the alloy is crucial to for the sensor long term-reliability.

2.3.1 Pd-Au and Pd-Cu Binary Alloys

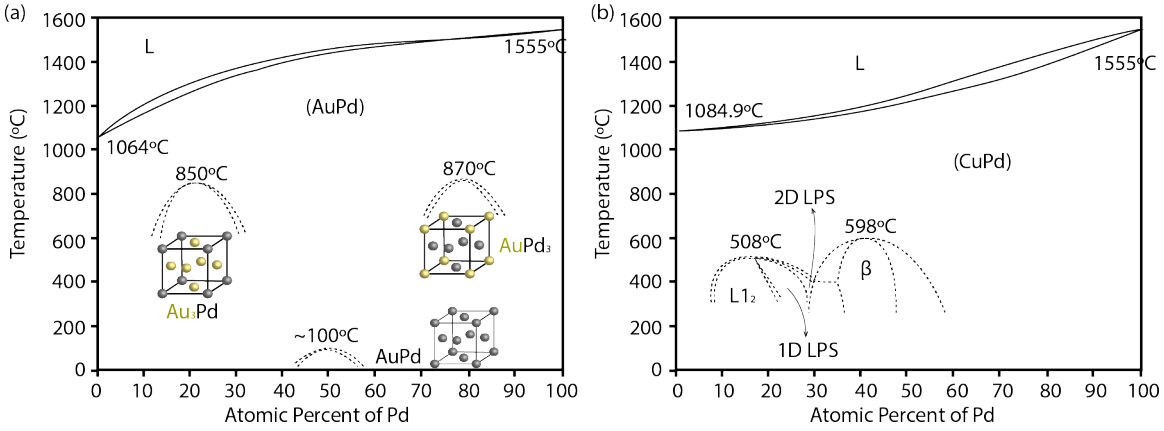

Figure 7: (a) Bulk Pd-Au and (b) Pd-Cu alloy phase diagrams (adapted from[142,143]).

Pd-Au alloys are known as white gold in jewelry and they form because Pd and Au are perfectly miscible. The corresponding equilibrium phase diagram is shown in *Figure 7a*. As can be seen, a PdAu solid solution exists and has an fcc crystal structure. In two small regions at high temperature below the solidus phase boundary, it forms an intermetallic phase with fcc crystal structure between 12-32 at.% Pd (Au_3Pd) and between 68-90 at.% Pd ($AuPd_3$)[142]. The corresponding unit cells of these structures are depicted in the figure. Since the lattice parameter of Au is larger than of Pd (a_{Au} = 4.078Å[144], a_{Pd} = 3.887Å[132]), the PdAu alloy lattice constant increases linearly according to Vegard's law with increasing Au content[142].

The equilibrium phase diagram of the Pd-Cu alloy system is presented in *Figure 7b.* PdCu alloys exist in fcc form across most of the phase diagram. At higher Cu contents, however, different structures appear. Specifically, when the Pd atomic percentage is in the range of 36-

47%, the alloy has a bcc crystal structure. Interestingly, this specific phase also possesses high permeability towards hydrogen[145]. At even higher Cu contents, a 1D anti-phase domain [APD] (17-28 at.-% Pd), a 2D APD (19-31 at.-% Pd), and Cu_3Pd $L1_2$ (7.6-22 at.-% Pd) exist[143]. In contrast to the PdAu system, PdCu shows a decreasing lattice parameter as the Cu content is increased[140]. The reason behind this trend is that the lattice parameter of Cu is smaller than the one of Pd (a_{Cu} = 3.627 Å[143], a_{Pd} = 3.887 Å[132]).

2.3.2 Pd-Cu-Au Ternary Alloy

In one of the articles included in this thesis, we have developed a ternary PdAuCu alloy to combine the best features of both binary PdAu and PdCu alloys for plasmonic hydrogen sensor applications. Thus, it is motivated to add some information about this alloy also here. Specifically, ternary PdAuCu alloys have been established mainly driven by the development of hydrogen separation membranes[146–150] using a number of techniques, namely arc melting[146], pulsed laser deposition[148], magnetron co-sputtering[147], multilayer electroless plating[149], and mechanical alloying[150]. For Cu-poor alloys, PdAuCu systems appear as fcc crystals, dictated by the fcc structure of PdAu. In binary PdCu, it is known that also bcc crystal structures exists when the Cu content is in the range of 53-64 at.-%. Hence, Cu-rich PdAuCu ternary alloys exhibit a bcc structure. According to Guerreiro *et al.*[150], the bcc structure is obtained when the alloy composition is 30 % ≤ Pd ≤ 46 %, 45 % ≤ Cu ≤ 63 % and 0 % ≤ Au ≤ 17%; with Pd+Cu+Au = 100 %. Finally, also the PdAuCu ternary alloys system lattice constant obeys Vegard's law, which means that it depends linearly on both the Cu and Au constituents.

2.3.3 Surface Segregation

For alloys systems, the concentrations of the alloy constituents in the bulk and at the surface are not necessarily identical due to surface segregation effects. Hence, surface segregation may have significant implications for the catalytic activity and thus, sensing function. To this end, it is well known that Pd alloys exhibit surface segregation, with the segregation depth profile being both monotonous and oscillatory. For example, using density functional theory (DFT) calculations, Løvvik has shown that PdCu alloys exhibit the latter type of depth profile, which may explain why in some cases the surface is rich in Pd while in other cases it is Cu-rich[151]. Other calculations predict that, in vacuum, Au has a higher tendency to segregate to the surface than Cu[151,152].

Mechanistically, there are multiple factors that may induce surface segregation, for instance geometrical effects (i.e. atomic radius of the constituents) and electronic effects[151,152]. Accordingly, DFT calculations on Pd alloys by Løvvik show that alloyant atoms of larger diameter than that of Pd (except Cu, Mn, and Rh) have a strong tendency to migrate to surfaces[151]. In the same reports, Løvvik also concludes that alloyants of lower surface energy than that of Pd (except Cu and Mn) are inclined to segregate onto the alloy surface. Furthermore, external conditions such as temperature and certain gases have an impact on surface segregation. For example, surface segregation less likely occurs at high temperature due to energy compensation, and since gases adsorb more strongly on certain metals than others, the gas environment's impact is a direct consequence of the combination of gas and elements in the alloy[151,152]. In hydrogen rich atmospheres as relevant here, the surface tends to be Pd rich due to the high affinity to hydrogen of Pd[152]. Similarly, in the presence of O_2 and H_2S, Cu tends to surface segregate in ternary PdAuCu systems[150]. Interestingly, CO

adsorption can also induce segregation of Pd to the surface of PdAg, PdCu, and PdAu alloys since it adsorbs strongly on Pd[152,153]. This fact is relevant to consider since the Pd alloy sensors we develop here are exposed to CO in the poisoning/cross-sensitivity tests.

3 Hydrogen Sensing Test Setups

In this chapter, I discuss the two kinds of setups I have used for testing the hydrogen sensing characteristics of the materials I have developed.

- **A vacuum chamber** for sensor kinetics and isotherm measurements.
- **Insplorion X1 flow reactor** for cross-sensitivity and poisoning tests.

3.1 Vacuum Chamber for Sensor Kinetics

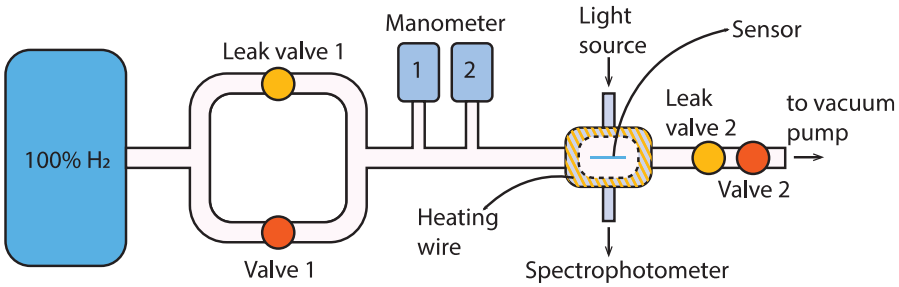

Figure 8: Schematic of the custom-built vacuum chamber hydrogen sensor test setup.

A schematic of the vacuum chamber hydrogen sensing setup is presented in *Figure 8.* The setup is connected to a pure 100% hydrogen source on one end and to a turbo vacuum pump on the other end. The hydrogen sensor chip is positioned in the center of the chamber. Hydrogen pressure in the chamber is controlled by either a leak valve or a standard valve. The leak valve is utilized to control the hydrogen pressure with high accuracy, as required when measuring pressure-composition isotherms. For sensor kinetics tests, a standard Nupro

valve is utilized instead, since it can be opened essentially instantaneously. The chamber pressure is monitored by two capacitance manometers (MKS Barathron 626C) of different pressure range. The first manometer is used to monitor 1-1000 mbar pressure while the second one is for 1-1000 μbar.

The chamber is wrapped by a heating coil and the temperature inside is monitored by a thermocouple attached to the hydrogen sensor chip. The heater and the thermocouple are connected to Eurotherm thermocontroller, which controls the chamber temperature in a feedback-loop manner. The chamber has two quartz windows which enable optical extinction measurements through the sensor using a fiber-coupled polychromatic halogen light source (Avantes AvaLight-Hal) and a fixed-grating spectrophotometer (Avantes SensLine AvaSpec-2048XL).

3.2 Insplorion X1 Flow Reactor

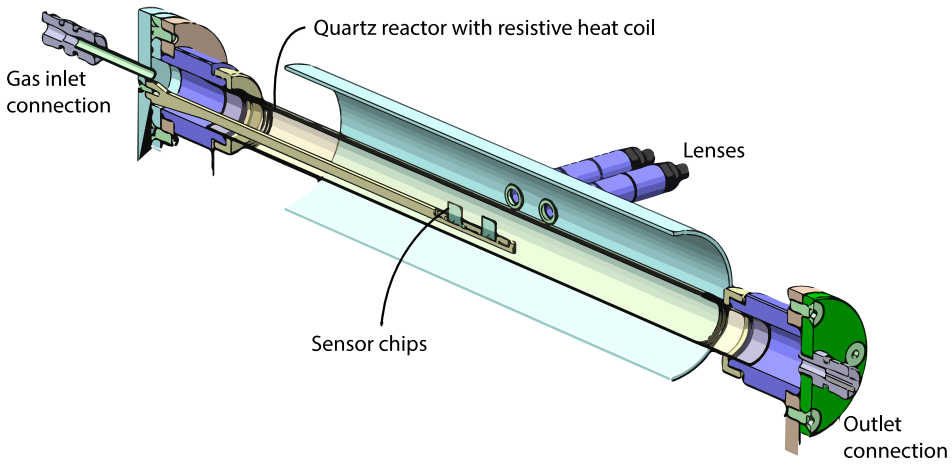

Figure 9: Insplorion X1 flow reactor (adapted with permission from Insplorion AB).

The sensor chip is positioned inside a resistive-heating-coil-wrapped quartz tube. The backside of sensor chip touches the thermocouple tip. Similar to the vacuum chamber, the

reactor temperature is controlled in feedback loop manner by a Eurotherm temperature controller. The temperature can be set up to 600˚C.

The gas inlet is connected to different gases controlled by mass flow controllers (Bronkhorst ΔP). The connected gases are O_2, CO_2, CO, NO_2 and CH_4. The X1 reactor is also connected to a humidifier which water generates vapor by mixing water and carrier gas in a Bronkhorst Controlled Evaporator Mixer (CEM).

The response of the sensor is monitored through the extinction spectrum. The spectrum is recorded and fitted by Insplorer® software which employs 20^{th} order polynomial fitting.

4 Nanofabrication by Hole-Mask Colloidal Lithography

There are two different approaches to create a nanosized material. The first one is to start with smaller units or building blocks (e.g. atoms, molecules) and to employ self-assembly of these units to form larger structures. The second strategy is to begin with a larger structure and craft it into smaller (nanosized) pieces. The former approach is known as *bottom-up* nanofabrication, whereas the latter one is known as *top-down* nanofabrication. An example of the bottom-up route for producing nanoparticles is the colloidal synthesis of Au nanoparticles from precursors in solution. In contrast, nanolithography is one of many techniques that fall into the top-down category.

Both bottom-up and top-down routes have advantages and disadvantages. For example, bottom-up approaches are in general less expensive since they typically require less sophisticated instrumentation. However, from the yield and reproducibility perspective, bottom-up is more problematic than top-down. On the other hand, top-down is usually more expensive since a sophisticated nanofabrication facility is needed. To this end, often a large fraction of nanofabrication cost is created by the preparation of the so-called mask. In photolithography, for instance, a mask is prepared with electron beam lithography, which writes the mask-pattern in serial fashion.

On the basis of this brief introduction, the main motivation for developing colloidal lithography nanofabrication that I used in this thesis work, was to eliminate the disadvantages of both routes. This is achieved by, in colloidal lithography, replacing the e-beam patterned mask with a mask created via the electrostatic self-assembly of polystyrene nanobeads on a surface[154–156]. Although the freedom to pattern arbitrary shapes provided by this approach is inherently inferior compared to an e-beam patterned mask, there has been a lot of creative nanostructure shapes successfully made with this method e.g. nanocrescents, nanotriangles, nanopillars, nanocones or nanoshuttlecocks[154,157–159]. Furthermore, in principle, colloidal lithography enables the formation of nanostructures from any material that can be evaporated. One powerful variant of colloidal lithography is the so-called hole-mask colloidal lithography (HCL) developed by Fredriksson *et al.*[160] where they, as the key step, introduced a sacrificial polymer layer to the fabrication. It is this method that I have used to make all nanostructures discussed in this thesis, by following the step-by-step recipe presented below.

4.1 Mask Preparation

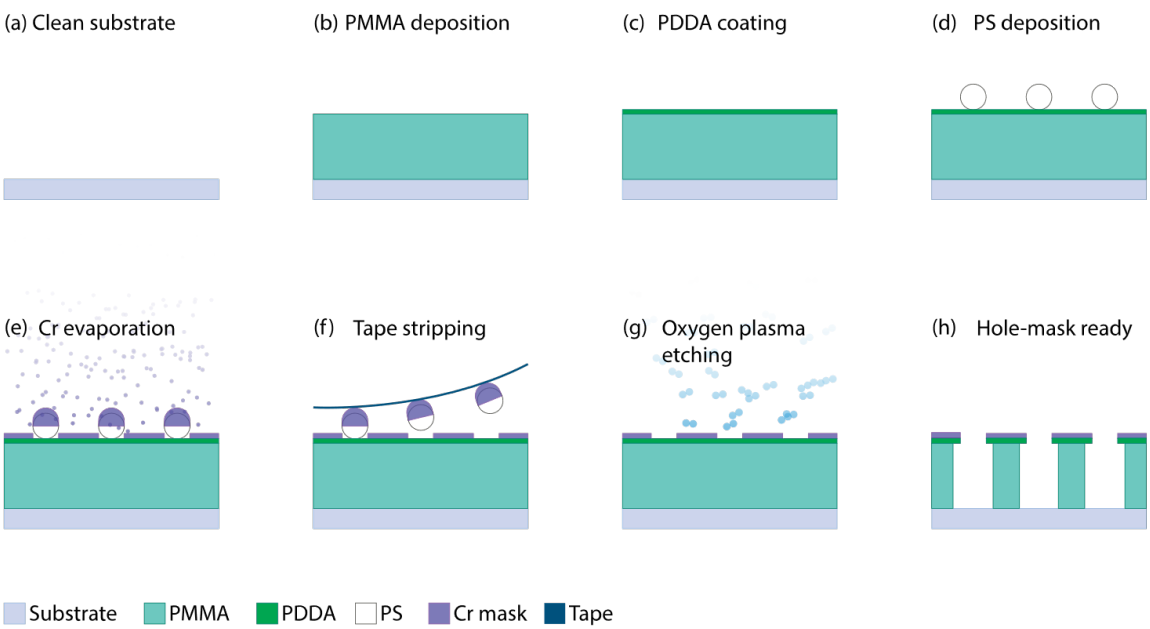

Figure 10: Hole-mask preparation steps in chronological order: (a) substrate preparation/cleaning, (b) PMMA sacrificial layer spin-coating, (c) application of positively-charged PDDA polyelectrolyte coating, (d) electrostatic self-assembly of PS nanobeads, (e) chromium mask evaporation, (f) tape stripping of PS nanobeads to create holes in the chromium mask, (g) oxygen plasma etch of the PMMA layer through the hole-mask. The final developed mask is illustrated in (h).

A schematic illustration of the entire hole-mask preparation sequence is presented in *Figure 10*, and below I provide some more detailed information about the individual steps:

(a) The substrate (typically fused silica or a silicon wafer) is cleaned subsequently with isopropanol (IPA), acetone, methanol, and IPA. Cleaning with each solvent is performed for 1 minute in an ultrasonicator. The purpose of this cleaning is to remove dust or any organic contaminant on the substrate.

(b) PMMA sacrificial layer deposition by spin-coating and subsequent soft-baking. We use anisole-diluted PMMA A4 solution (Mw = 950 000) for this purpose. The

substrate is placed on a spinner and few drops of PMMA solution are applied on to the substrate. An approximately 200 nm thick PMMA film is then obtained by spinning at 2000 rpm for 60 seconds. Afterwards, the coated substrate is soft-baked at 170˚C for 3 minutes to evaporate the remaining solvent.

(c) Positively-charged poly(diallyldimethylammonium chloride) (PDDA) solution is drop-coated onto the PMMA sacrificial layer. PDDA is purchased from Sigma Aldrich (Mw =100 000-200 000 diluted in 20% H_2O) and diluted in water to achieve 0.2 wt.% concentration. Prior to PDDA drop coating, the PMMA layer is exposed to oxygen plasma (50 W, 250 Torr, 10 sccm) for 5 seconds to reduce surface hydrophobicity. The drop coated PMMA is then incubated for 1 minute followed by washing with Milli-Q water for 10 seconds and nitrogen blow-dry.

(d) Negatively-charged polystyrene (PS) nanobeads are drop cast onto the PDDA-coated PMMA sacrificial layer. The original PS nanobead stock-solutions were purchased from Life Technology and diluted in Milli-Q water to 0.2 wt% concentration. The diluted PS solution is then drop coated and incubated for 2 minutes to enable the self-assembly of a scarce monolayer of PS beads on the surface, followed by a rinse in Milli-Q 10 seconds. The sample is later dried with nitrogen blow.

(e) 15 nm Chromium mask growth by e-beam physical vapor deposition (PVD).

(f) Tape stripping to remove the nanobeads, leaving holes in the Chromium mask where the PMMA now is exposed.

(g) 5 min oxygen plasma etch (50 W, 250 Torr, and 10 sccm) to transfer the hole-pattern into the PMMA.

(h) The final structure of the hole-mask.

4.2 Material Deposition

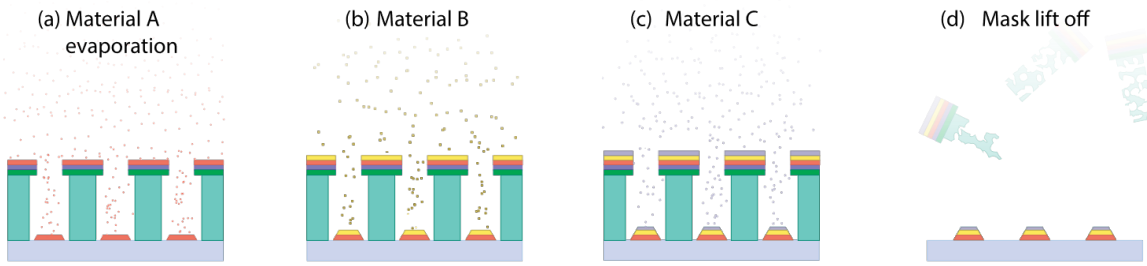

Figure 11: Material(s) deposition through hole-mask and annealing illustration. One or more materials can be evaporated through the mask by e-beam PVD. Illustrated in (a)→(c): metal A, B, and C are sequentially deposited. Afterwards, the mask is lifted-off with organic solvent, leaving only the nanodisk structures on the surface (d).

After the hole-mask is prepared, material deposition through the mask is performed by using e-beam PVD. If desired, multiple materials can be evaporated subsequently through the mask to, for example, enable the fabrication of layered structures or alloys (*Figure 11*). After the material deposition step, the mask together with all material deposited on top of it, is removed in a lift-off step by dissolving the PMMA in an organic solvent such as Acetone. This yields a quasi-random array of disk-like nanoparticles on the surface. As the last step for the case of the fabrication of alloy nanoparticles that I have done in this thesis a thermal annealing in reducing atmosphere (4% H_2 in Ar) is carried out at 500˚C for 24 hours to ensure homogeneous alloy formation from subsequently deposited layers of the alloy constituents[60,161].

5 Nanofabrication Tools

In this chapter I describe in more detail the key tools I have used for my sample nanofabrication based on hole-mask colloidal lithography:

- Spin coating: to develop the PMMA sacrificial layer.
- Electron beam physical vapor deposition: to develop the metallic lithography mask and to deposit material through the mask.
- Plasma reactive ion etching: to transfer the mask pattern into the PMMA sacrificial layer by oxygen plasma etching.

5.1 Spin Coating

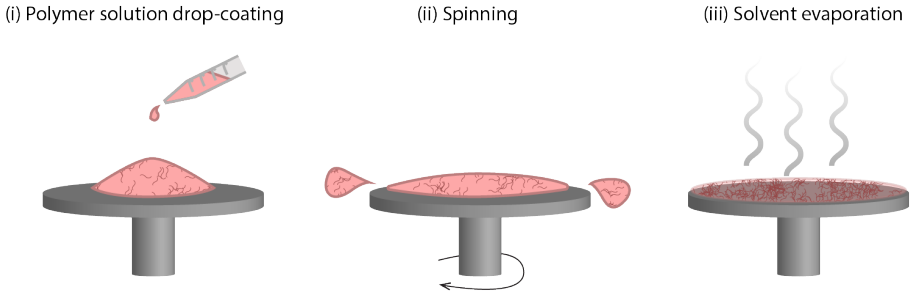

Figure 12: Polymer deposition by spin coating technique. The three main steps are (i) drop-coating of solvent-diluted polymer, (ii) spinning to create centrifugal force that removes excess solution, and (iii) evaporation to remove the solvent.

Spin coating is a relatively cheap yet very effective technique to deposit polymer thin films. Illustrated in *Figure 12*, the major steps of the spin coating process are (i) drop casting of polymer solution on the substrate, (ii) substrate spinning with defined acceleration and

rotation speed to create the centrifugal force needed to evenly spread the solution on the surface, (iii) soft-baking to remove excess solvent.

Despite the apparent simplicity, spin coating can sometimes be difficult since its successful application is dictated by several factors. From the perspective of the polymer itself, its characteristics, such as molecular weight/chain length or polarity, are important factors to consider. For example, heavy/long molecules will form a thicker layer[162,163]. Furthermore, it has been also reported that different solvents may result in different polymer structures and thus properties of the spin coated films and that the concentration of the polymer in the solvent dictates the film thickness (via viscosity), where a more diluted solution tends to make thinner films[162,163]. For a given polymer solution, the film thickness (t) can be controlled by the angular spin speed (ω): $t \propto \frac{1}{\sqrt{\omega}}$. Solvent evaporation occurs continuously during spinning and the subsequent soft-baking. The latter is done either in an oven or on a hotplate at temperatures above solvent boiling point but below the polymer decomposition temperature.

5.2 Electron Beam Physical Vapor Deposition

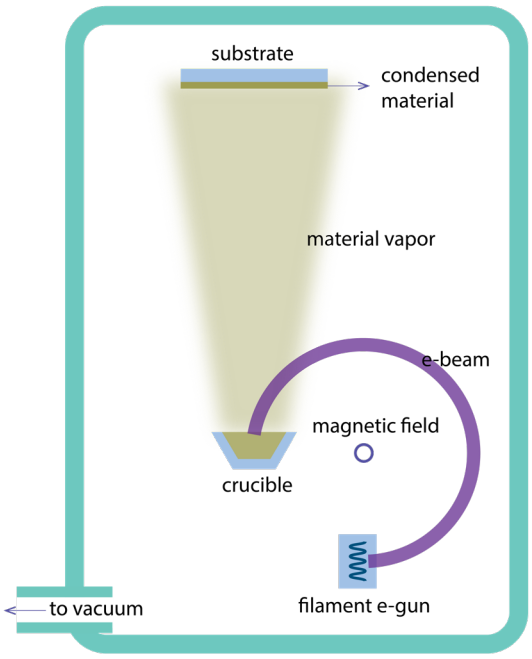

Figure 13: Schematic of electron-beam physical vapor deposition. Electrons are generated by a heated-filament gun directed by a perpendicular magnetic field onto the material source. The heated material evaporates towards the substrate placed above the crucible. Material vapor adsorbs on the substrate and condenses to form a thin film.

As illustrated in *Figure 13*, the main steps of e-beam PVD are (i) heating of the source material by the electron beam in vacuum environment, (ii) material transport to substrate through vacuum in "line of sight", and (iii) material condensation on the substrate[164]. The evaporation process itself is induced by the fact that at increasing source temperature, its vapor pressure increases. The rate of deposition of monomers from the source then correlates with vapor pressure. Hence, to deposit material with reasonable rate, a certain vapor pressure has to be achieved. To this end, the vapor pressure vs. temperature relation depends on the material at hand. For example, tungsten (W) requires extremely high temperatures above 3000˚C to attain reasonable vapor pressure while other metals such as Au, Ag, and Cu are

evaporated at lower temperatures due to their considerably lower melting temperatures. To monitor the deposition rate, a PVD system is usually equipped with a quartz crystal microbalance (QCM). The PVD process is done in vacuum, which is critical since a too high chamber pressure may lead to contamination of the deposited materials with, for example, oxygen.

5.3 Plasma-enhanced Reactive Ion Etching

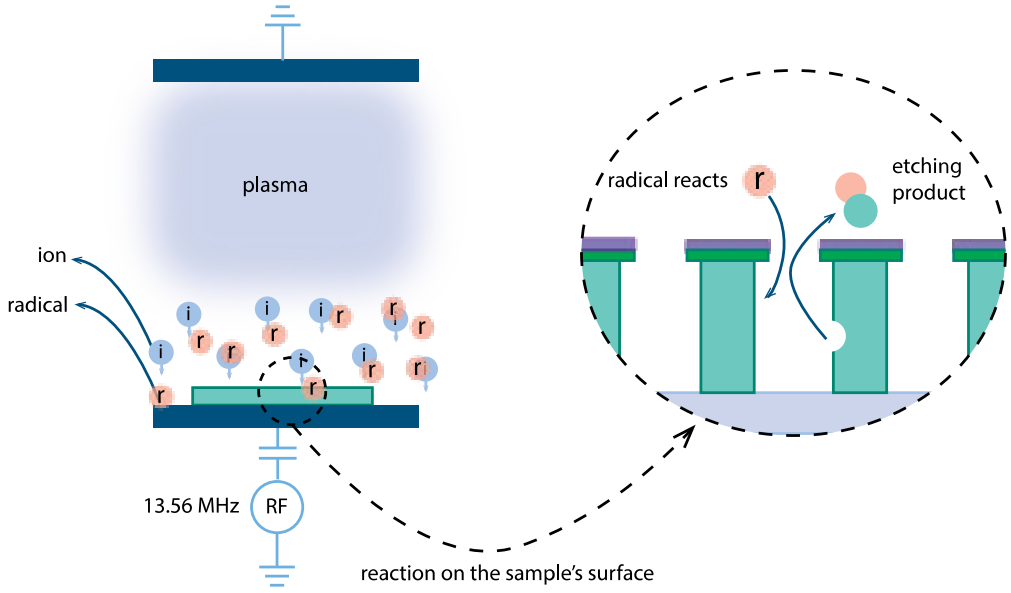

Figure 14: Schematic of plasma-enhanced reactive ion-etching process[165]*. Plasma is generated in between the two electrodes. The anode is connected to a 13.56 MHz radio-frequency generator. Plasma is comprised of both gas ions and radicals. In the inset, reactive radical adsorbs onto the sample surface to promote the etching reaction. In this case, I relate the illustration to the etching process of the PMMA sacrificial layer explained earlier in the hole-mask colloidal lithography process in Figure 10.*

When a gas is localized between two electrodes, the electric field will induce separation of positive and negative charges, while maintaining zero net charge. At this condition, the gas transforms into plasma. To give a concrete example for how plasma-assisted etching works,

let me illustrate oxygen plasma formation and how it can be used for etching of a solid material. Oxygen (O_2) flows between the two electrodes, which are connected to an external RF (radio frequency) source. The electric field inside the chamber then creates a cloud of plasma, i.e. separated ions (O^+) and electrons (e^-). Subsequently, the electrons collide with further O_2 molecules to produce oxygen radicals (O_2*). These radicals have much longer lifetime than oxygen ions created directly by the charge separation and are thus more abundant in the chamber. The formed radicals then diffuse towards the sample surface and react chemically with it, thereby removing material if a gaseous species is formed (e.g. upon reaction of hydrocarbons with the plasma, forming CO_2). It is also worth mentioning that not only chemical etching process may occur. Physical sputtering might simultaneously take place due to ion bombardment driven by the electric field.

For this process, the etch rate and profile depend on several factors, such as process pressure and RF power. High process pressure leads to a larger amount of radicals and thus increases the etch rate and selectivity. With high process pressure, the gas mean-free-path decreases and thus the etching profile becomes more isotropic. The RF power is proportional to the number of created radicals and ions. More radicals imply higher etching rate but at the same time reduces selectivity due to ionic sputtering. Higher RF power also leads to more isotropic etching due to a stronger vertical electric field.

6 Material Characterization

After the nanofabrication process is completed, characterization of the samples is necessary to confirm the desired nanostructure has been achieved. This is important for the interpretation of the samples' sensing performance. We use electron-based microscopy for the characterization. The material characterization techniques used in my project together with the corresponding purpose are:

- Scanning electron microscopy (SEM): main purpose is to obtain images of the fabricated nanoparticle arrays. From such images, nanostructure size distribution and surface coverage can be calculated.
- Energy-dispersive x-ray spectroscopy (EDS/EDX): main purpose is to obtain information of the elemental composition of sample, such as of the Pd-based alloys studied in this thesis.
- X-Ray photoelectron spectroscopy (XPS): main purpose is to measure the elemental surface composition of the nanofabricated samples, as well as surface oxidation state and surface segregation effects.
- Quartz crystal microbalance (QCM): main purpose is to quantify the amount of hydrogen absorption by the fabricated Pd (alloy) nanostructures.

6.1 Scanning Electron Microscopy (SEM)

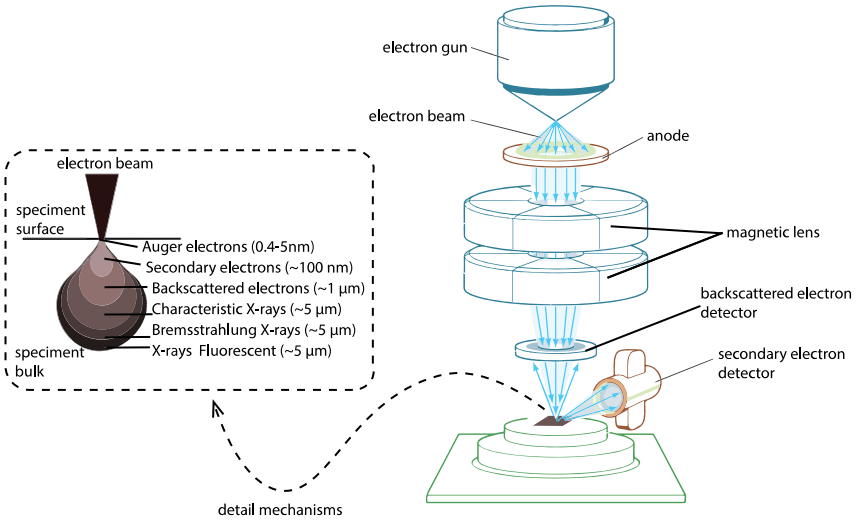

Figure 15: Schematic of a scanning electron microscope and the profile of the generated signal from the sample surface (adapted and modified from refs.[166,167]*).*

The key components of a SEM unit are the electron gun, magnetic lenses, scan coils, and the electron detector (*Figure 15*). There are two kinds of electron guns i.e. thermionic and field emission guns (FEG). Thermionic guns generate electrons via thermal excitation of a metal (e.g. tungsten), while a FEG creates the electron beam via a strong electric field. A FEG beam outperforms a thermionic gun by significantly higher electron intensity and narrower energy spread (thus better image resolution). The FEG, however, has a higher cost. The electron beam created from the gun is directed to sample surface by two magnetic lenses: the condenser and the objective lens. The condenser lens focuses the electrons emitted by the source before it enters the objective aperture. Here, a strong condenser lens is needed to ensure that the electron beam does not spread too widely. Right before the beam enters the objective lens, its direction is controlled with the scanning coil. Finally, the objective lens focuses the beam onto the sample surface. When impinging on the surface, the electron beam induces the emission of multiple types of particles and photons, including X-rays, visible

photons (cathodoluminescence), secondary electrons (SE) and backscattered electrons (BSE). As indicated in *Figure 15*, these different products are all generated at different sample surface depths. SEs are generated close to the surface and, thus, carry surface (topography) information. BSEs are emitted from deeper inside the sample (bulk).

Like any other microscopy technique, the ultimate aim of SEM is to obtain the best possible image resolution. To achieve this, there are many factors to consider. For example, since the sample surface is flooded with electrons during imaging, the sample has to be sufficiently conductive to transfer excess charge to ground. Hence, to obtain an image with high resolution from an insulating sample (e.g. glass) is usually more difficult than from a metal. Similarly, the used acceleration voltage of the electron beam is important for the obtained resolution. Higher acceleration voltage leads to deeper electron penetration on the sample surface which also broadens the interaction volume. This broadening means that the scattered electron signal comes from larger area which consequently reduces the lateral resolution[166,168]. The working distance (i.e. distance between objective lens and sample surface) determines the depth of focus and a shorter working distance means increase of depth of focus. Hence, to have the right working distance is crucial for imaging structures with high aspect ratio and for imaging at an angle. Finally, good resolution is enabled only when the microscope chamber pressure is sufficiently low to minimize electron scattering from molecules in the chamber.

For the SEM imaging, I used a Zeiss Supra 60 VP and I prepared the imaged nanostructures on reasonably conducting silicon substrates to minimize charging effects. As the typical working distance I used 5 mm, together with an accelerating voltage of 10-15 kV.

6.2 Energy Dispersive X-Ray Spectroscopy (EDS/EDX)

EDS is a very useful spectroscopy method that can be combined with electron microscopy. In principle, one can simply add an X-ray detector to an electron microscope to perform EDS since, as depicted in *Figure 15*, X-rays are produced upon impact of the electron beam on the specimen. These X-rays stem from a volume that extends approximately 5 μm below the specimen surface and there are two kinds of generated X-rays: characteristic X-rays and Bremsstrahlung.

Bremsstrahlung is the product of the beam electrons kinetic energy loss due to interaction with the atomic cores of the specimen. Characteristic X-rays are generated by electronic transitions of the specimen's atoms upon interaction with the incoming electron beam. Specifically, the beam knocks a core electron from its orbital, therefore creating a hole. Consequently, an electron from an outer orbital undergoes transition to occupy the available core hole. This transition releases characteristic X-ray quanta, which are used to identify the elements present in the specimen. For EDS, only characteristic X-rays are of interest. EDS can be used for both qualitative and quantitative analysis. However, there are limitations such as peak overlap, poor energy resolution (~100 eV) and difficulties to detect lighter elements.

6.3 X-Ray Photoelectron Spectroscopy (XPS)

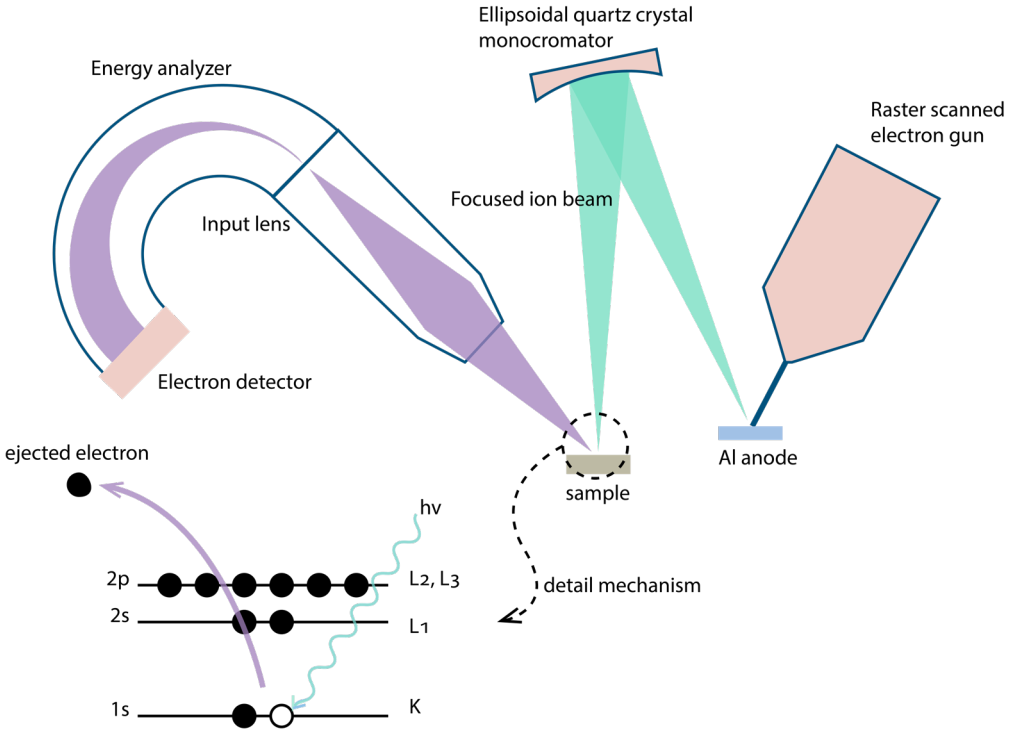

Figure 16: Schematic depiction and mechanism of X-ray photoelectron spectroscopy (XPS) simplified from [169].

XPS enables non-destructive surface characterization of a material down to 0.5-10 nm of depth (depending strongly on the material) and composition detection of 0.1-1 atomic percent[170,171]. The working principle is as follows. Electron gun generated electrons are directed towards a metallic source, e.g. Al. The electron - metal interaction generates X-rays. In the case of an Al source, typically the generated characteristic X-ray energy is 1486.6 eV (Al Kα)[172]. The X-rays are then directed on to the sample surface and knock out a core electron to the vacuum level, leaving behind a core hole (*Figure 16*). Accordingly, dictated by the simple energy conservation principle, the core electron binding energy, BE, can be expressed as:

$$BE = h\nu - KE, \qquad eq.\ 4$$

where hν and KE is the kinetic energy of the ejected electrons. By analyzing the kinetic energy of ejected electrons, one can thus obtain the core electron binding energy. Since the core electron binding energies are unique for each element of the periodic table, it is used for surface elemental analysis. Furthermore, small shifts in binding energy *generally* contains information about, for example, the oxidation state of the surface. The oxide has higher binding energy than its metallic counterpart because the valence electron is drawn towards the oxygen atom, which leads to a more positively charged core. This more positive core, thus, increases attraction to the remaining electrons[172]. Practically, shifts towards higher BE usually means increasing oxidation state, while shift towards lower BE means more reduced state. For example, the $3d_{5/2}$ peak of PdO is 336.4 eV, which is higher than metallic Pd's 335.4 eV[173].

For my work, I have used a PHI 5000 XPS system and preferably samples prepared on a conducting substrate such as Si. For XPS analysis of samples on an insulating substrate (e.g. fused silica), a charge neutralizer was used. As reference for the energy scale, I used the carbon 1s peak by shifting the entire spectrum to match the carbon 1s standard value of 384.5 eV.

6.4 Quartz Crystal Microbalance (QCM)

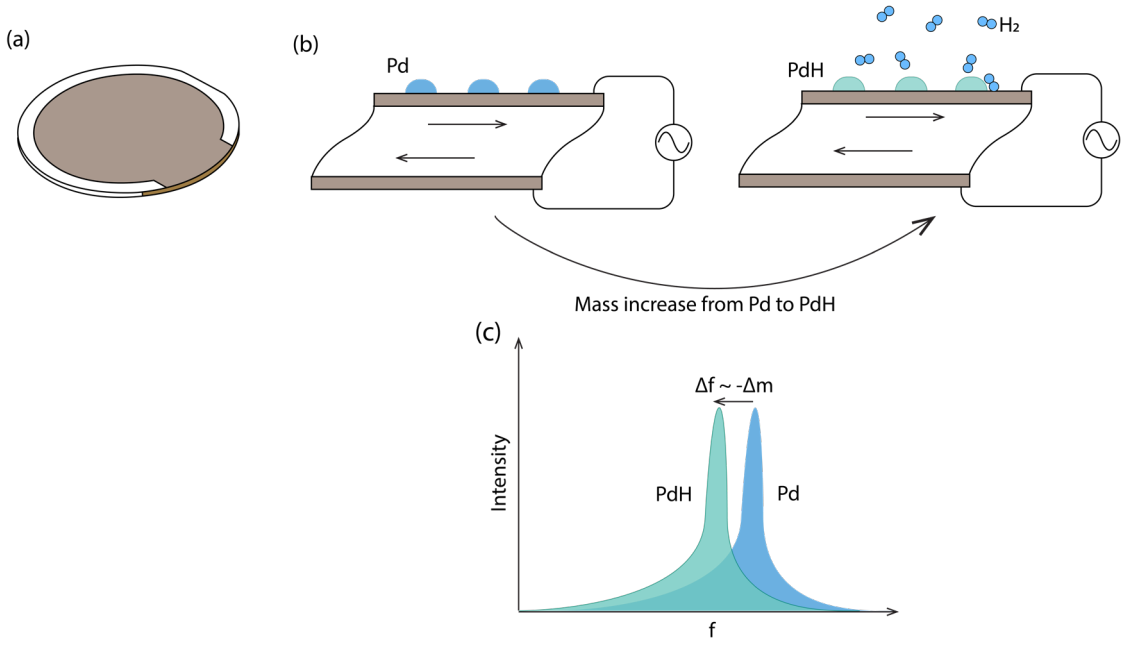

Figure 17: *Quartz crystal microbalance. (a) The QCM sensor consists of a quartz disc with a Au electrode deposited on each side. (b) An applied external AC bias drives a shear oscillation of the QCM crystal. For my project, I deposited Pd alloy nanoparticles on the QCM crystal. The resonance frequency change of this shear oscillation is proportional to the change of mass on the QCM sensor, i.e. the mass of the hydrogen absorbed by the Pd alloy. (c) Typical response of the QCM sensor. Over the frequency sweep (f), there is a peak that corresponds to the crystal's resonance frequency. The frequency shift (Δf) is proportional to the mass change on the crystal (Δm).*

I have used QCM to quantify the amount of hydrogen absorbed by Pd and Pd alloy nanoparticles, and to correlate this information with their optical LSPR response (**Paper III**). The QCM is basically a highly sensitive scale that employs a simple harmonic oscillation principle, where the resonance frequency change (Δf) scales linearly with the change in mass per unit area (Δm) on the resonator. This relation is formally known as Sauerbrey equation[174]:

$$\Delta f = -C_f \Delta m, \qquad \textit{eq. 5}$$

where C_f is the sensitivity factor that depends on the used crystal type. For the 10 MHz SC-cut crystals I have used in this work, C_f is 4.8 ng cm^{-2} Hz^{-1}. The QCM instrument unit I used is a QSense Explorer by Biolin Scientific.

7 Summary and outlook

I hereby summarize the four appended papers, make a critical review to my work and make an outlook.

7.1 Summary

- ***Paper I****: Rationally-Designed PdAuCu Ternary Alloy Nanoparticles for Intrinsically Deactivation-Resistant Ultrafast Plasmonic Hydrogen Sensing.*

  The work was motivated by the fact that Pd-based hydrogen sensors are prone to CO poisoning. We adapted a well-known strategy from hydrogen separation membrane technology to improve Pd's resistance to CO poisoning by alloying with Cu. We found that a small amount of Cu addition (5 at.%) to Pd vastly improves the poisoning resistance. At the same time, sensitivity is decreased for increasing Cu content and hysteresis persists up to 30 at.%.

  To alleviate the sensitivity and hysteresis problem, while at the same time preserving the poisoning resistance, we combined PdCu with another binary alloy system – PdAu – introduced for plasmonic hydrogen sensing by Wadell *et al.*[60] They reported that 25 at.% Au addition to Pd eliminates Pd hysteresis and improves the response time of the corresponding sensor. As the key result of this paper, by combining these two binary systems, we were able to develop a ternary PdAuCu nanoplasmonic hydrogen sensor that possesses the best features of the constituents: it is hysteresis-free, has fast response/recovery time, and is resistant to carbon-monoxide poisoning.

- ***Paper II****: Metal-polymer Hybrid Nanomaterials for Plasmonic Ultrafast Hydrogen Detection.*

  In this article we report as the main finding that the combination of a PTFE/PMMA tandem coating and PdAu alloy nanoparticles enables a poisoning resistant and highly sensitive hydrogen sensor with ultrafast response time. In the paper, we systematically investigated all the constituents to derive the system that performs the best. Specifically, we begun the work by testing a PTFE coating on a PdAu nanoplasmonic hydrogen sensor and found that the polymer coating reduces the hydrogen absorption time *via* an activation energy reduction. We also observed nearly double sensitivity *via* refractive index far-field plasmonic enhancement. In the deactivation tests, however, the PTFE did not protect the PdAu nanoparticles from CO poisoning.

  Hence, as an alternative, we then tested PMMA-coated PdAu. Similar to the PTFE, sensitivity and response time enhancement were achieved, despite the completely different polymer chemistry of PTFE and PMMA. The PMMA response time enhancement, however, was inferior to PTFE's. This finding is supported by apparent activation energy measurements and DFT calculations. Furthermore, in the deactivation tests, the PMMA-PdAu system showed excellent resistance towards CO-poisoning.

  Finally, we then combined those two polymer systems into a "tandem" PTFE/PMMA coating on top of PdAu alloy nanoparticles, in which the PTFE is responsible for the maximal response time enhancement through activation energy reduction at the Pd-PTFE interface, while the PMMA is in charge of deactivation protection by filtering out poisoning gases.

- ***Paper III****: Universal Scaling and Design Rules of Hydrogen-Induced Optical Properties in Pd and Pd-Alloy Nanoparticles.*

  In this article, we performed simultaneous optical (LSPR) and gravimetric (QCM) studies of Pd alloy (i.e. PdAu and PdCu) nanoparticle interactions with hydrogen. The gravimetric measurements for particles with varied alloyant-concentration revealed that only the Pd part of the alloy is responsible for hydrogen absorption. Furthermore, we discovered that the LSPR descriptors, i.e. change of peak position, extinction at peak, and full-width of half-maximum, scale linearly with the relative hydrogen concentration (H/Pd) in the system, independent of the alloy composition. In this work, we also revealed that the optical "hydrogen sensitivity" depends only on the LSPR peak spectral position of the non-hydrogenated state, and not on the absolute amount of absorbed hydrogen.

  We interpret these findings as "universal design rules" for metal-hydride-based plasmonic hydrogen sensors, which are important to consider for real device optimization. Moreover, these findings also provide deeper insight in the mechanism of hydrogen sensing by plasmonic nanostructures.

- ***Paper IV****: The Impact of Surfactants and Stabilizers on Pd Nanoparticle Surface Catalyzed Reactions with Hydrogen.*

  This paper is motivated by our interest in utilizing colloidally-synthesized Pd nanoparticles for plasmonic hydrogen sensing. Synthesized Pd nanoparticles are inevitably covered by surfactants, which are crucial for both size/shape control during

synthesis and to prevent particle aggregation in solution. Since the Pd nanoparticle surface state is crucial for both hydrogen absorption and desorption, we investigated the effect of four different commonly used surfactants adsorbed on the Pd surface. In contrast to earlier reports, we prepared non-surfactant stabilized nanoparticles via hole-mask colloidal lithography on a surface, which we then coated with the desired surfactant by drop-casting. We tested the effect of four different surfactants/stabilizer commonly used in Pd nanoparticle synthesis: cetrimonium bromide (CTAB), tetraoctylamonium bromide (TOAB), cetrimonium chloride (CTAC), and polyvinylpyrrolidone (PVP) on the hydrogenation kinetics of Pd.

The key findings of the study are: (i) the cationic surfactants (CTAB, CTAC, TOAB) decelerate the hydrogen (de)absorption kinetics, while the polymeric stabilizer PVP accelerates it. (ii) For the cationic surfactants, the deceleration effect is dictated by both halide-atom interaction with Pd as identified by DFT calculations, and by the alkyl-chain packing density. (iii) The surfactants/stabilizers do not completely deactivate Pd's hydrogen sorption ability. (iv) For hydrogen sensing applications, the choice of surfactant is important with respect to optimizing the sensor response time.

7.2 Critical Review of The Results

Here, I critically review the work included in this thesis in order to identify and briefly discuss its limitations and drawbacks.

Paper I

- In the limit of detection (LoD) tests (*Figure 4* in the manuscript), the sensor was still responsive at 10 μbar hydrogen pressure (the lowest value reliably possible in the used setup). The recorded peak shift and noise level were 0.1 nm and 0.01 nm, respectively. Given that the plasmonic peak of Pd alloy nanoparticles is very broad

(hundreds nanometer of FWHM) and the wavelength resolution of the spectrophotometer is 1 nm, the (much) smaller peak shift and noise level needs to be investigated further.

- In the stability test of the ternary sensor, the sensor showed stability from two aspects: response/recovery time and absence of oxidation/surface segregation, as shown by XPS analysis (*Figure 5e-f* in the manuscript). The test procedure was as follows. Once every two weeks, I measured the sensor's kinetics followed by XPS analysis. There is drawback of this testing method. The absence of the oxidation/surface segregation might be caused by the reducing effect of hydrogen during the kinetics test. In other words, segregation may still have occurred but was reversed by hydrogen exposure. Moreover, it is also not so accurate to say that the sensor is stable for seven weeks because the sample is exposed to hydrogen (thus it is "refreshed") every two weeks. Therefore a modified test where multiple sensors are used and only tested once should be performed.
- It is still not clear why only 5% of additional Cu makes significant improvement on the CO-poisoning resistance. Further investigation is necessary to answer this question.
- The sensor performance was tested at constant room temperature, while the DOE standard (*Table 2*) requires a broader range of operational temperature. It is still an open question how the sensor perform under extremely high and low temperature.

Paper II

- The sensor showed extremely fast response. However, the test was performed in a vacuum chamber, which is not realistic for application. Further upgrade of the test reactor is necessary to simulate close to realistic conditions.

- Same issue as for **Paper I**, the sensor showed remarkable sensitivity and noise level, which are several decades lower than the plasmonic peak FWHM and spectrophotometer wavelength resolution.
- Same issue as for **Paper I**, where the sensor performance was tested only at room temperature.

Paper IV

- For the kinetics and activation energy comparison we prepared five similar samples Pd, Pd@CTAB, Pd@CTAC, Pd@TOAB, and Pd@PVP where Pd is used as a baseline. The sample-to-sample variation between those samples might contribute to the inaccuracy of the comparison. Ideally one should compare the kinetics of coated and uncoated Pd of the same sample.

7.3 Outlook

There are several outlook-points that indicate the future directions of my work, which I would like to summarize as follows.

- In **Paper I** and **Paper II** we have demonstrated the excellent response time of our hydrogen sensors. The tests, however, were performed in a vacuum/pure hydrogen, which is not a realistic application condition. I will thus "upgrade" our sensing test setup to enable response time tests in synthetic air background in the presence of poisoning gases to mimic real application conditions.
- Since long-term stability of a sensor is crucial, I will also carry out a systematic examination of both structural stability (e.g. alloy segregation, polymer protection) and of the sensing performance over time at the months to year time scale.
- Despite its excellent performance, in paper I, I only present one PdAuCu ternary alloy composition. In the next step, we will thus investigate the hydrogen sensing characteristics of PdAuCu in a more systematic manner by varying the alloy-

constituent concentration. We will also merge the PdAuCu system with polymer coatings that we have tested successfully on PdAu. Moreover, paper I also leaves interesting questions on why merely 5 at.% Cu is sufficient to "protect" Pd from poisoning. I believe that the answer to this question is worth to investigate, either with theoretical calculations or experimentally by in-situ surface mapping techniques such as Raman or FTIR, or both.

- With more insights on the Pd-polymer (**Paper II**) and the Pd-surfactant (**Paper III**) interactions at hand, we will explore a more scalable route to produce Pd-polymer nanocomposites. The route will be to use colloidally synthesized Pd nanoparticles and to embed them into a polymer matrix.

8 Acknowledgements

First of all, I acknowledge the funding support from the Swedish Foundation for Strategic Research Framework project RMA15-0052.

I always feel grateful to be able to work in this very supportive team and working environment. I would have not been able to come this far without contribution of these people and I want to thank them:

- My supervisor, Christoph Langhammer, thank you for your positive encouragement and guidance.
- My co-supervisor Christian Müller and examiner Henrik Grönbeck for the discussion and feedbacks.
- Ferry Nugroho who I work closely with and who always is available for help and discussion.
- All Langhammer group members and former members. I really appreciate your support and the good time with you.
- All member of SSF Plastic Plasmonic project. Particularly Ida, Alicja, and Lucy who I collaborate closely with.
- All my collaborators I really appreciate but cannot mention all their names one by one here.
- Chemical Physics members for the good time, discussions and help.
- Chalmers MC2 cleanroom staff.

And finally, I would thank the great support from outside my professional life:

- My teachers
- My friends
- My family

9 References

1. Fraile, D., Lanoix, J.-C., Maio, P., Rangel, A. & Torres, A. *Overview of the market segmentation for hydrogen across potential customer groups, based on key application areas*. (2015).
2. Cigal, J.-C. Expanding use of hydrogen in the electronics industry. *Specialty Gas Report* 26 (2016).
3. Hydrogen in electronics: growing applications and consumptions. *www.semiconductor.net* 26–31 (2017).
4. Boon-Brett, L. *et al.* Identifying performance gaps in hydrogen safety sensor technology for automotive and stationary applications. *Int. J. Hydrogen Energy* **35,** 373–384 (2010).
5. Crabtree, G. W., Dresselhaus, M. S. & Buchanan, M. V. The Hydrogen Economy. *Phys. Today* **57,** 39–44 (2004).
6. Morgan, T. The hydrogen economy - A non-technical Review. *United Nations Environment Programme* (2006). Available at: www.unep.fr/energy/. (Accessed: 17th May 2017)
7. Züttel, A., Remhof, A., Borgschulte, A. & Friedrichs, O. Hydrogen: the future energy carrier. *Philos. Trans. R. Soc. A Math. Phys. Eng. Sci.* **368,** 3329–3342 (2010).
8. Liu, K., Song, C. & Subramani, V. *Hydrogen and Syngas Production and Purification Technologies*. (John Wiley & Sons, Inc., 2009). doi:10.1002/9780470561256
9. Muller, R. *Physics for future presidents : the science behind the headlines*. (W. W. Norton & Company, 2009).
10. Muller, R. *Energy for future presidents: the science behind the headlines*. *W. W. Norton & Company* (W. W. Norton & Company, 2013).
11. Hoagland, B. *Hydrogen leak detection – low cost distributed gas sensors*. (2012).
12. Sansone, F. J. Fuel cell hydrogen sensor for marine applications. *Mar. Chem.* **37,** 3–14 (1992).
13. Leonardi, S. G., Bonavita, A., Donato, N. & Neri, G. Development of a hydrogen dual sensor for fuel cell applications. *Int. J. Hydrogen Energy* **43,** 11896–11902 (2018).
14. Hübert, T., Boon-Brett, L. & Buttner, W. J. *Sensors for safety and process control in*

hydrogen technologies. (CRC Press, 2016).

15. Hübert, T., Boon-Brett, L., Black, G. & Banach, U. Hydrogen sensors - A review. *Sensors Actuators, B Chem.* **157,** 329–352 (2011).
16. Hoffheins, B. S., McKnight, T. E., Lauf, R. J., Smith, R. R. & James, R. E. *Evaluation of a hydrogen sensor for nuclear reactor containment monitoring*. *International topical meeting on advanced reactor safety, Orlando, FL (United States), 1-4 Jun 1997* (Oak Ridge National Laboratory, 1997). doi:10.2172/486067
17. Hach Company. *Analysis Of Waste-Gas / Off-Gas Oxygen and Hydrogen in Nuclear Power Plants*. (2015).
18. Yang, F., Jung, D. & Penner, R. M. Trace Detection of Dissolved Hydrogen Gas in Oil Using a Palladium Nanowire Array. *Anal. Chem.* **83,** 9472–9477 (2011).
19. Pavlovsky, I. Hydrogen Sensor for Oil Transformer Health Monitoring. in *2008 8th IEEE Conference on Nanotechnology* 211–213 (IEEE, 2008). doi:10.1109/NANO.2008.69
20. Sun, C., Ohodnicki, P. R. & Stewart, E. M. Chemical Sensing Strategies for Real-Time Monitoring of Transformer Oil: A Review. *IEEE Sens. J.* **17,** 5786–5806 (2017).
21. Cheng, J., Wang, C. & Zhang, S. Methods to determine the mine gas explosibility – An overview. *J. Loss Prev. Process Ind.* **25,** 425–435 (2012).
22. Franks, R. ., Friel, G. ., Edwards, J. . & Smith, A. . In-mine evaluation of smart mine fire sensor. in *Society for Mining, Metallurgy and Exploration - SME Annual Meeting and Exhibit 2008: 'New Horizons - New Challenges'* 332–338 (Society for Mining, Metallurgy, and Exploration, 2008).
23. Rana, S. V. & Malik, A. Hydrogen Breath Tests in Gastrointestinal Diseases. *Indian J. Clin. Biochem.* **29,** 398–405 (2014).
24. Olson, J. W. & Maier, R. J. Molecular hydrogen as an energy source for Helicobacter pylori. *Science* **298,** 1788–90 (2002).
25. Grimes, C. A. *et al.* A Sentinel Sensor Network for Hydrogen Sensing. *Sensors* **3,** 69–82 (2003).
26. Cleland, N., Hörnsten, E. G., Elwing, H., Enfors, S. O. & Lundström, I. Measurement of hydrogen evolution by oxygen-limited E. coli by means of a hydrogen sensitive Pd-MOS sensor. *Appl. Microbiol. Biotechnol.* **20,** 268–270 (1984).
27. Vignais, P. M. & Colbeau, A. Molecular biology of microbial hydrogenases. *Current Issues in Molecular Biology* **6,** 159–188 (2004).
28. Harrison, D. K. & Kessler, M. A multiwire hydrogen electrode for in vivo use. *Phys.*

Med. Biol. **34,** 1397–1412 (1989).

29. Ohsawa, I. *et al.* Hydrogen acts as a therapeutic antioxidant by selectively reducing cytotoxic oxygen radicals. *Nat. Med.* **13,** 688–694 (2007).
30. Ohta, S. Recent progress toward hydrogen medicine: potential of molecular hydrogen for preventive and therapeutic applications. *Curr. Pharm. Des.* **17,** 2241–52 (2011).
31. Zhao, D., Wang, T. & Heineman, W. R. Advances in H2 sensors for bioanalytical applications. *TrAC Trends Anal. Chem.* **79,** 269–275 (2016).
32. Kuhlmann, J. *et al.* Fast escape of hydrogen from gas cavities around corroding magnesium implants. *Acta Biomater.* **9,** 8714–8721 (2013).
33. Hitchcock, C. H. S. Determination of hydrogen in irradiated frozen chicken. *J. Sci. Food Agric.* **68,** 319–323 (1995).
34. Hitchcock, C. H. . Determination of hydrogen as a marker in irradiated frozen food. *J. Sci. Food Agric.* **80,** 131–136 (2000).
35. Hübert, T., Boon-Brett, L., Palmisano, V. & Bader, M. A. Developments in gas sensor technology for hydrogen safety. *Int. J. Hydrogen Energy* **39,** 20474–20483 (2014).
36. Korotcenkov, G., Han, S. Do & Stetter, J. R. Review of Electrochemical Hydrogen Sensors. *Chem. Rev.* **109,** 1402–1433 (2009).
37. Gu, H. *et al.* Hydrogen Gas Sensors Based on Semiconductor Oxide Nanostructures. *Sensors* **12,** 5517–5550 (2012).
38. McKeown, S. J., Wang, X., Yu, X. & Goddard, L. L. Realization of palladium-based optomechanical cantilever hydrogen sensor. *Microsystems Nanoeng.* **3,** 16087 (2017).
39. Jang, B., Lee, K. Y., Noh, J. S. & Lee, W. Nanogap-based electrical hydrogen sensors fabricated from Pd-PMMA hybrid thin films. *Sensors Actuators, B Chem.* **193,** 530–535 (2014).
40. Lee, J., Shim, W., Lee, E., Noh, J. S. & Lee, W. Highly mobile palladium thin films on an elastomeric substrate: Nanogap-based hydrogen gas sensors. *Angew. Chemie - Int. Ed.* **50,** 5301–5305 (2011).
41. Kiefer, T., Villanueva, L. G., Fargier, F., Favier, F. & Brugger, J. Fast and robust hydrogen sensors based on discontinuous palladium films on polyimide, fabricated on a wafer scale. *Nanotechnology* **21,** 505501 (2010).
42. Nugroho, F. A. A., Darmadi, I., Zhdanov, V. P. & Langhammer, C. Universal Scaling and Design Rules of Hydrogen-Induced Optical Properties in Pd and Pd-Alloy Nanoparticles. *ACS Nano* **12,** 9903–9912 (2018).
43. Christofides, C. & Mandelis, A. Operating characteristics and comparison of

photopyroelectric and piezoelectric sensors for trace hydrogen gas detection. II. Piezoelectric quartz-crystal microbalance sensor. *J. Appl. Phys.* **66,** 3986–3992 (1989).

44. Sil, D., Hines, J., Udeoyo, U. & Borguet, E. Palladium Nanoparticle-Based Surface Acoustic Wave Hydrogen Sensor. *ACS Appl. Mater. Interfaces* **7,** 5709–5714 (2015).
45. Palm, K. J., Murray, J. B., Narayan, T. C. & Munday, J. N. Dynamic Optical Properties of Metal Hydrides. *ACS Photonics* **5,** 4677–4686 (2018).
46. Boelsma, C. *et al.* Hafnium - An optical hydrogen sensor spanning six orders in pressure. *Nat. Commun.* **8,** 15718 (2017).
47. Radeva, T. *et al.* Highly sensitive and selective visual hydrogen detectors based on Y xMg1-x thin films. *Sensors Actuators, B Chem.* **203,** 745–751 (2014).
48. Dam, B., Ngene, P., Bras, W., Longo, A. & Mooij, L. Metal-hydrogen systems with an exceptionally large and tunable thermodynamic destabilization. *Nat. Commun.* **8,** 1846 (2017).
49. van Well, A. A. *et al.* Optical hydrogen sensing beyond palladium: Hafnium and tantalum as effective sensing materials. *Sensors Actuators B Chem.* **283,** 538–548 (2018).
50. Gremaud, R. *et al.* Hydrogenography: An optical combinatorial method to find new light-weight hydrogen-storage materials. *Adv. Mater.* **19,** 2813–2817 (2007).
51. Liu, P. *et al.* Stable Pd/V2O5 Optical H2 Sensor. *J. Electrochem. Soc.* **149,** H76 (2002).
52. Kalanur, S. S., Lee, Y.-A. & Seo, H. Eye-readable gasochromic and optical hydrogen gas sensor based on CuS–Pd. *RSC Adv.* **5,** 9028–9034 (2015).
53. Schreuders, H., Radeva, T., Ngene, P., Westerwaal, R. & Dam, B. Eye readable metal hydride based hydrogen tape sensor for health applications. in *Photonics Applications for Aviation, Aerospace, Commercial, and Harsh Environments V* (eds. Kazemi, A. A., Kress, B. C. & Mendoza, E. A.) **9202,** 920203 (International Society for Optics and Photonics, 2014).
54. The H2Sense Hydrogen Sensor Database. Available at: https://netzwerke.bam.de/Netzwerke/Content/EN/Downloads/h2sense-database.pdf?__blob=publicationFile. (Accessed: 10th March 2019)
55. Fisser, M., Badcock, R. A., Teal, P. D. & Hunze, A. Optimizing the sensitivity of palladium based hydrogen sensors. *Sensors Actuators, B Chem.* **259,** 10–19 (2018).
56. Penner, R. M. A Nose for Hydrogen Gas: Fast, Sensitive H2 Sensors Using Electrodeposited Nanomaterials. *Acc. Chem. Res.* **50,** 1902–1910 (2017).

57. Walter, E. C., Favier, F. & Penner, R. M. Palladium mesowire arrays for fast hydrogen sensors and hydrogen-actuated switches. *Anal. Chem.* **74,** 1546–1553 (2002).
58. Xu, T. *et al.* Self-assembled monolayer-enhanced hydrogen sensing with ultrathin palladium films. *Appl. Phys. Lett.* **86,** 203104 (2005).
59. Westerwaal, R. J. *et al.* Nanostructured Pd–Au based fiber optic sensors for probing hydrogen concentrations in gas mixtures. *Int. J. Hydrogen Energy* **38,** 4201–4212 (2013).
60. Wagner, J. B. *et al.* Hysteresis-Free Nanoplasmonic Pd–Au Alloy Hydrogen Sensors. *Nano Lett.* **15,** 3563–3570 (2015).
61. Nugroho, F. A. A., Eklund, R., Nilsson, S. & Langhammer, C. A fiber-optic nanoplasmonic hydrogen sensor via pattern-transfer of nanofabricated PdAu alloy nanostructures. *Nanoscale* **10,** 20533–20539 (2018).
62. Yamazaki, H., Hayashi, Y., Masunishi, K., Ono, D. & Ikehashi, T. High sensitivity MEMS capacitive hydrogen sensor with inverted T-shaped electrode and ring-shaped palladium alloy for fast response and low power consumption. *J. Micromechanics Microengineering* **28,** 094001 (2018).
63. Hayashi, Y., Yamazaki, H., Ono, D., Masunishi, K. & Ikehashi, T. Investigation of PdCuSi metallic glass film for hysteresis-free and fast response capacitive MEMS hydrogen sensors. *Int. J. Hydrogen Energy* **43,** 9438–9445 (2018).
64. Morreale, B. D. *et al.* Effect of hydrogen-sulfide on the hydrogen permeance of palladium-copper alloys at elevated temperatures. *J. Memb. Sci.* **241,** 219–224 (2004).
65. Kamakoti, P. *et al.* Prediction of hydrogen flux through sulfur-tolerant binary alloy membranes. *Science* **307,** 569–73 (2005).
66. Palmisano, V. *et al.* Selectivity and resistance to poisons of commercial hydrogen sensors. *Int. J. Hydrogen Energy* **40,** 11740–11747 (2015).
67. O'Brien, C. P. Sulfur Poisoning of Pd and PdCu Alloy Hydrogen Separation Membranes. (Carnegie Mellon Univsersity, 2011).
68. Sakai, H., Nakajima, T., Yoshida, N. & Kishimoto, S. Poisoning effect of carbon monoxide on the desorption process of hydrogen from palladium. *React. Kinet. Catal. Lett.* **19,** 297–301 (1982).
69. Liu, J. *et al.* Tackling CO Poisoning with Single-Atom Alloy Catalysts. *J. Am. Chem. Soc.* **138,** 6396–6399 (2016).
70. Baselt, D. R. *et al.* Design and performance of a microcantilever-based hydrogen sensor. *Sensors Actuators B Chem.* **88,** 120–131 (2003).

71. Offermans, P. *et al.* Ultralow-power hydrogen sensing with single palladium nanowires. *Appl. Phys. Lett.* **94,** 223110 (2009).
72. Zhang, D., Sun, Y., Jiang, C. & Zhang, Y. Room temperature hydrogen gas sensor based on palladium decorated tin oxide/molybdenum disulfide ternary hybrid via hydrothermal route. *Sensors Actuators, B Chem.* **242,** 15–24 (2017).
73. Luo, X. *et al.* Rapid hydrogen sensing response and aging of A-MoO3 nanowires paper sensor. *Int. J. Hydrogen Energy* **42,** 8399–8405 (2017).
74. Sanger, A., Jain, P. K., Mishra, Y. K. & Chandra, R. Palladium decorated silicon carbide nanocauliflowers for hydrogen gas sensing application. *Sensors Actuators, B Chem.* **242,** 694–699 (2017).
75. Zhang, H., Yi, J. & Jiang, X. Fast Response, Highly Sensitive and Selective Mixed-Potential H2 Sensor Based on (La, Sr)(Cr, Fe)O3-δ Perovskite Sensing Electrode. *ACS Appl. Mater. Interfaces* **9,** 17218–17225 (2017).
76. Hassan, K. & Chung, G. S. Fast and reversible hydrogen sensing properties of Pd-capped Mg ultra-thin films modified by hydrophobic alumina substrates. *Sensors Actuators, B Chem.* **242,** 450–460 (2017).
77. Moon, J., Hedman, H.-P., Kemell, M., Tuominen, A. & Punkkinen, R. Hydrogen sensor of Pd-decorated tubular TiO2 layer prepared by anodization with patterned electrodes on SiO2/Si substrate. *Sensors Actuators B Chem.* **222,** 190–197 (2016).
78. Sanger, A., Kumar, A., Kumar, A. & Chandra, R. Highly sensitive and selective hydrogen gas sensor using sputtered grown Pd decorated MnO2 nanowalls. *Sensors Actuators, B Chem.* **234,** 8–14 (2016).
79. Hassan, K., Iftekhar Uddin, A. S. M. & Chung, G. S. Fast-response hydrogen sensors based on discrete Pt/Pd bimetallic ultra-thin films. *Sensors Actuators, B Chem.* **234,** 435–445 (2016).
80. Woo, J. A., Phan, D. T., Jung, Y. W. & Jeon, K. J. Fast response of hydrogen sensor using palladium nanocube-TiO2 nanofiber composites. *Int. J. Hydrogen Energy* **42,** 18754–18761 (2017).
81. Xiang, C. *et al.* A room-temperature hydrogen sensor based on Pd nanoparticles doped TiO 2 nanotubes. *Ceram. Int.* **40,** 16343–16348 (2014).
82. Hong, J. *et al.* A highly sensitive hydrogen sensor with gas selectivity using a PMMA membrane-coated Pd nanoparticle/single-layer graphene hybrid. *ACS Appl. Mater. Interfaces* **7,** 3554–3561 (2015).
83. Chen, M. *et al.* Response Characteristics of Hydrogen Sensors Based on PMMA-

Membrane-Coated Palladium Nanoparticle Films. *ACS Appl. Mater. Interfaces* **9,** 27193–27201 (2017).

84. Venkatesan, A. *et al.* Molybdenum disulfide nanoparticles decorated reduced graphene oxide: Highly sensitive and selective hydrogen sensor. *Nanotechnology* **28,** 365501 (2017).
85. Favier, F., Walter, E. C., Zach, M. P., Benter, T. & Penner, R. M. Hydrogen sensors and switches from electrodeposited palladium mesowire arrays. *Science (80-.).* **293,** 2227–2231 (2001).
86. Hu, J. *et al.* Highly sensitive and ultra-fast gas sensor based on CeO2-loaded In2O3 hollow spheres for ppb-level hydrogen detection. *Sensors Actuators, B Chem.* **257,** 124–135 (2018).
87. Nugroho, F. A. A. *et al.* Metal - Polymer Hybrid Nanomaterials for Plasmonic Ultrafast Hydrogen Detection. *Nat. Mater.* **in press,** (2019).
88. Gautam, Y. K., Chandra, R., Kumar, A., Sanger, A. & Chauhan, S. Fast and reversible hydrogen sensing properties of Pd/Mg thin film modified by hydrophobic porous silicon substrate. *Sensors Actuators B Chem.* **213,** 252–260 (2015).
89. Li, X., Liu, Y., Hemminger, J. C. & Penner, R. M. Catalytically Activated Palladium@Platinum Nanowires for Accelerated Hydrogen Gas Detection. *ACS Nano* **9,** 3215–3225 (2015).
90. Perrotton, C. *et al.* A reliable, sensitive and fast optical fiber hydrogen sensor based on surface plasmon resonance. *Opt. Express* **21,** 382 (2013).
91. Kumar, M. *et al.* Efficient room temperature hydrogen sensor based on UV-activated ZnO nano-network. *Nanotechnology* **28,** 365502 (2017).
92. Kim, T. H. *et al.* Palladium Nanoribbon Array for Fast Hydrogen Gas Sensing with Ultrahigh Sensitivity. *Adv. Mater.* **27,** 6945–6952 (2015).
93. Monzón-Hernández, D., Luna-Moreno, D. & Martínez-Escobar, D. Fast response fiber optic hydrogen sensor based on palladium and gold nano-layers. *Sensors Actuators B Chem.* **136,** 562–566 (2009).
94. Hassan, K., Uddin, A. S. M. I., Ullah, F., Kim, Y. S. & Chung, G. S. Platinum/palladium bimetallic ultra-thin film decorated on a one-dimensional ZnO nanorods array for use as fast response flexible hydrogen sensor. *Mater. Lett.* **176,** 232–236 (2016).
95. Zhao, H. *et al.* Optical fiber hydrogen sensor based on an annealing-stimulated Pd–Y thin film. *Sensors Actuators B Chem.* **216,** 11–16 (2015).

96. Chen, W. P. *et al.* Extraordinary room-temperature hydrogen sensing capabilities of porous bulk Pt-TiO2 nanocomposite ceramics. *Int. J. Hydrogen Energy* **41,** 3307–3312 (2016).
97. Cho, S. Y. *et al.* Ultrasmall Grained Pd Nanopattern H2Sensor. *ACS Sensors* **3,** 1876–1883 (2018).
98. Koo, W.-T. *et al.* Accelerating Palladium Nanowire H 2 Sensors Using Engineered Nanofiltration. *ACS Nano* **11,** 9276–9285 (2017).
99. Kumar, R. *et al.* Fast detection and low power hydrogen sensor using edge-oriented vertically aligned 3-D network of MoS 2 flakes at room temperature . *Appl. Phys. Lett.* **111,** 093102 (2017).
100. Rajoua, K., Baklouti, L. & Favier, F. Electronic and mechanical antagonist effects in resistive hydrogen sensors based on Pd@Au core-shell nanoparticle assemblies prepared by Langmuir-Blodgett. *J. Phys. Chem. C* **119,** 10130–10139 (2015).
101. Shim, Y. S. *et al.* Nanogap-controlled Pd coating for hydrogen sensitive switches and hydrogen sensors. *Sensors Actuators, B Chem.* **255,** 1841–1848 (2018).
102. Hughes, R. C. & Schubert, W. K. Thin films of Pd/Ni alloys for detection of high hydrogen concentrations. *J. Appl. Phys. J. Appl. Phys.* **71,** (1992).
103. He, J. *et al.* Integrating plasmonic nanostructures with natural photonic architectures in Pd-modified *Morpho* butterfly wings for sensitive hydrogen gas sensing. *RSC Adv.* **8,** 32395–32400 (2018).
104. Chen, R., Ruan, X., Liu, W. & Stefanini, C. A reliable and fast hydrogen gas leakage detector based on irreversible cracking of decorated palladium nanolayer upon aligned polymer fibers. *Int. J. Hydrogen Energy* **40,** 746–751 (2015).
105. Lim, S. H. *et al.* Flexible palladium-based H2 sensor with fast response and low leakage detection by nanoimprint lithography. *ACS Appl. Mater. Interfaces* **5,** 7274–7281 (2013).
106. Seo, J., Lim, Y. & Shin, H. Self-heating hydrogen gas sensor based on an array of single suspended carbon nanowires functionalized with palladium nanoparticles. *Sensors Actuators, B Chem.* **247,** 564–572 (2017).
107. Xia, X. *et al.* A hydrogen sensor based on orientation aligned TiO2thin films with low concentration detecting limit and short response time. *Sensors Actuators, B Chem.* **234,** 192–200 (2016).
108. Lupan, O. *et al.* Ultra-sensitive and selective hydrogen nanosensor with fast response at room temperature based on a single Pd/ZnO nanowire. *Sensors Actuators, B Chem.*

254, 1259–1270 (2018).

109. Uddin, A. S. M. I. & Chung, G. S. A self-powered active hydrogen gas sensor with fast response at room temperature based on triboelectric effect. *Sensors Actuators, B Chem.* **231,** 601–608 (2016).
110. Yoo, H.-W., Cho, S.-Y., Jeon, H.-J. & Jung, H.-T. Well-Defined and High Resolution Pt Nanowire Arrays for a High Performance Hydrogen Sensor by a Surface Scattering Phenomenon. *Anal. Chem.* **87,** 1480–1484 (2015).
111. Jang, J. S. *et al.* Hollow Pd-Ag Composite Nanowires for Fast Responding and Transparent Hydrogen Sensors. *ACS Appl. Mater. Interfaces* **9,** 39464–39474 (2017).
112. Phan, D. T., Uddin, A. S. M. I. & Chung, G. S. A large detectable-range, high-response and fast-response resistivity hydrogen sensor based on Pt/Pd core-shell hybrid with graphene. *Sensors Actuators, B Chem.* **220,** 962–967 (2015).
113. Seo, D. K. *et al.* Flexible hydrogen sensors using graphene with palladium nanoparticle decoration. *Sensors Actuators B Chem.* **169,** 387–392 (2012).
114. Kiefer, T., Favier, F., Vazquez-Mena, O., Villanueva, G. & Brugger, J. A single nanotrench in a palladium microwire for hydrogen detection. *Nanotechnology* **19,** 125502 (2008).
115. Mayer, K. M. & Hafner, J. H. Localized Surface Plasmon Resonance Sensors. *Chem. Rev.* **111,** 3828–3857 (2011).
116. Hao, E. & Schatz, G. C. Electromagnetic fields around silver nanoparticles and dimers. *J. Chem. Phys.* **120,** 357–366 (2004).
117. Lee, K.-S. & El-Sayed, M. A. Gold and Silver Nanoparticles in Sensing and Imaging: Sensitivity of Plasmon Response to Size, Shape, and Metal Composition. *J. Phys. Chem. B* **110,** 19220–19225 (2006).
118. Langhammer, C., Yuan, Z., Zorić, I. & Kasemo, B. Plasmonic Properties of Supported Pt and Pd Nanostructures. *Nano Lett.* **6,** 833–838 (2006).
119. Xu, W., Zhang, Y. & Chen, T. *Single Particle Nanocatalysis*. (Wiley-VCH Verlag GmbH & Co. KGaA, 2019). doi:10.1002/9783527809721
120. Wadell, C., Syrenova, S. & Langhammer, C. Plasmonic Hydrogen Sensing with Nanostructured Metal Hydrides. *ACS Nano* **8,** 11925–11940 (2014).
121. Silkin, V. M., Díez Muiño, R., Chernov, I. P., Chulkov, E. V & Echenique, P. M. Tuning the plasmon energy of palladium–hydrogen systems by varying the hydrogen concentration. *J. Phys. Condens. Matter* **24,** 104021 (2012).
122. El Matbouly, H. *et al.* Assessment of commercial micro-machined hydrogen sensors

performance metrics for safety sensing applications. *Int. J. Hydrogen Energy* **39,** 4664–4673 (2014).

123. Gao, X. *et al.* Visual detection of microRNA with lateral flow nucleic acid biosensor. *Biosens. Bioelectron.* **54,** 578–84 (2014).
124. Unser, S., Bruzas, I., He, J. & Sagle, L. Localized Surface Plasmon Resonance Biosensing: Current Challenges and Approaches. *Sensors (Basel).* **15,** 15684–716 (2015).
125. Kim, S.-W. *et al.* Easy-to-Fabricate and High-Sensitivity LSPR Type Specific Protein Detection Sensor Using AAO Nano-Pore Size Control. *Sensors* **17,** 856 (2017).
126. Bingham, J. M., Anker, J. N., Kreno, L. E. & Van Duyne, R. P. Gas Sensing with High-Resolution Localized Surface Plasmon Resonance Spectroscopy. *J. Am. Chem. Soc.* **132,** 17358–17359 (2010).
127. Chen, B., Liu, C., Xie, Y., Jia, P. & Hayashi, K. Localized Surface Plasmon Resonance Gas Sensor Based on Molecularly Imprinted Polymer Coated Au Nano-Island Films: Influence of Nanostructure on Sensing Characteristics. *IEEE Sens. J.* **16,** 3532–3540 (2016).
128. Joy, N. A. *et al.* Selective Plasmonic Gas Sensing: H 2 , NO 2 , and CO Spectral Discrimination by a Single Au-CeO 2 Nanocomposite Film. *Anal. Chem.* **84,** 5025–5034 (2012).
129. Nugroho, F. A. A. *et al.* Plasmonic Nanospectroscopy for Thermal Analysis of Organic Semiconductor Thin Films. *Anal. Chem.* **89,** 2575–2582 (2017).
130. Langhammer, C. & Larsson, E. M. Nanoplasmonic In Situ Spectroscopy for Catalysis Applications. *ACS Catal.* **2,** 2036–2045 (2012).
131. Knapton, A. G. Palladium Alloys for Hydrogen Diffusion Membranes. *Platin. Met. Rev.* **21,** 44–50 (1977).
132. Manchester, F. D., San-Martin, A. & Pitre, J. M. The H-Pd (hydrogen-palladium) System. *J. Phase Equilibria* **15,** 62–83 (1994).
133. Jimenez, G. *et al.* A Comparative Assessment of Hydrogen Embrittlement: Palladium and Palladium-Silver (25 Weight% Silver) Subjected to Hydrogen Absorption/Desorption Cycling. *Adv. Chem. Eng. Sci.* **06,** 246–261 (2016).
134. Volkov, A. Y., Novikova, O. S., Kostina, A. E. & Antonov, B. D. Effect of alloying with palladium on the electrical and mechanical properties of copper. *Phys. Met. Metallogr.* **117,** 945–954 (2016).
135. Nam, S.-E., Seong, Y.-K., Lee, J. W. & Lee, K.-H. Preparation of highly stable

palladium alloy composite membranes for hydrogen separation. *Desalination* **236,** 51–55 (2009).

136. Alique, D. *et al.* Review of Supported Pd-Based Membranes Preparation by Electroless Plating for Ultra-Pure Hydrogen Production. *Membranes (Basel).* **8,** 5 (2018).
137. Schwarz, R. B. & Khachaturyan, A. G. Thermodynamics of open two-phase systems with coherent interfaces: Application to metal–hydrogen systems. *Acta Mater.* **54,** 313–323 (2006).
138. Matuschek, M. *et al.* Chiral Plasmonic Hydrogen Sensors. *Small* 1702990 (2017). doi:https://doi.org/10.1002/smll.201702990
139. Lee, E. *et al.* Hydrogen gas sensing performance of Pd–Ni alloy thin films. *Thin Solid Films* **519,** 880–884 (2010).
140. Burch, R. & Buss, R. G. Absorption of hydrogen by palladium–copper alloys. Part 1.—Experimental measurements. *J. Chem. Soc. Faraday Trans. 1 Phys. Chem. Condens. Phases* **71,** 913 (1975).
141. Burch, R. & Buss, R. G. Absorption of hydrogen by palladium–copper alloys. Part 2.—Theoretical analysis. *J. Chem. Soc. Faraday Trans. 1 Phys. Chem. Condens. Phases* **71,** 922 (1975).
142. Okamoto, H. & Massalski, T. B. The Au−Pd (Gold-Palladium) system. *Bull. Alloy Phase Diagrams* **6,** 229–235 (1985).
143. Subramanian, P. . & Laughlin, D. . Cu-Pd (Copper-Palladium). *J. Phase Equilibria* **12,** 231–243 (1991).
144. Allison, E. G. & Bond, G. C. The Structure and Catalytic Properties of Palladium-Silver and Palladium-Gold Alloys. *Catal. Rev.* **7,** 233–289 (1972).
145. Zhang, K. & Way, J. D. Palladium-copper membranes for hydrogen separation. *Sep. Purif. Technol.* **186,** 39–44 (2017).
146. Sakamoto, Y., Ishimaru, N. & Mukai, Y. Thermodynamics of Solution of Hydrogen in Pd-Cu and Pd-Cu-Au Solid Solution Alloys. *Berichte der Bunsengesellschaft für Phys. Chemie* **95,** 680–688 (1991).
147. Honrado Guerreiro, B., Martin, M. H., Roué, L. & Guay, D. Hydrogen Solubility of Magnetron Co-Sputtered FCC and BCC PdCuAu Thin Films. *J. Phys. Chem. C* **120,** 5297–5307 (2016).
148. Galipaud, J., Martin, M. H., Roué, L. & Guay, D. Pulsed Laser Deposition of PdCuAu Alloy Membranes for Hydrogen Absorption Study. *J. Phys. Chem. C* **119,** 26451–

26458 (2015).

149. Jia, H. *et al.* High-temperature stability of Pd alloy membranes containing Cu and Au. *J. Memb. Sci.* **544,** 151–160 (2017).

150. Guerreiro, B. M. H. Palladium-Copper-Gold Alloys for the Separation of Hydrogen Gas. *Doctoral Thesis* (Université du Québec, 2015).

151. Løvvik, O. M. Surface segregation in palladium based alloys from density-functional calculations. *Surf. Sci.* **583,** 100–106 (2005).

152. Zhao, M., Sloof, W. G. & Böttger, A. J. Modelling of surface segregation for palladium alloys in vacuum and gas environments. *Int. J. Hydrogen Energy* **43,** 2212–2223 (2018).

153. O'Brien, C. P. & Lee, I. C. The interaction of CO with PdCu hydrogen separation membranes: An operando infrared spectroscopy study. *Catal. Today* (2017). doi:10.1016/j.cattod.2017.09.039

154. Colson, P., Henrist, C. & Cloots, R. Nanosphere Lithography: A Powerful Method for the Controlled Manufacturing of Nanomaterials. *J. Nanomater.* **2013,** 1–19 (2013).

155. Zhang, G. & Wang, D. Colloidal Lithography-The Art of Nanochemical Patterning. *Chem. - An Asian J.* **4,** 236–245 (2009).

156. Yu, Y. & Zhang, G. in *Updates in Advanced Lithography* **8,** 3–34 (InTech, 2013).

157. Syrenova, S., Wadell, C. & Langhammer, C. Shrinking-hole colloidal lithography: Self-aligned nanofabrication of complex plasmonic nanoantennas. *Nano Lett.* **14,** 2655–2663 (2014).

158. Ai, B., Möhwald, H., Wang, D. & Zhang, G. Advanced Colloidal Lithography Beyond Surface Patterning. *Adv. Mater. Interfaces* **4,** 1600271 (2017).

159. Yang, S.-M., Jang, S. G., Choi, D.-G., Kim, S. & Yu, H. K. Nanomachining by Colloidal Lithography. *Small* **2,** 458–475 (2006).

160. Dmitriev, A. *et al.* Hole–Mask Colloidal Lithography. *Adv. Mater.* **19,** 4297–4302 (2007).

161. Nugroho, F. A. A., Iandolo, B., Wagner, J. B. & Langhammer, C. Bottom-Up Nanofabrication of Supported Noble Metal Alloy Nanoparticle Arrays for Plasmonics. *ACS Nano* **10,** 2871–2879 (2016).

162. Das, R. & Chanda, A. in *Nano-size Polymers* 283–306 (Springer International Publishing, 2016). doi:10.1007/978-3-319-39715-3_10

163. Norrman, K., Ghanbari-Siahkali, A. & Larsen, N. B. 6 Studies of spin-coated polymer films. *Annu. Reports Sect. 'C' (Physical Chem.* **101,** 174 (2005).

164. Gatzen, H. H., Saile, V. & Leuthold, J. in *Micro and Nano Fabrication* 65–203 (Springer Berlin Heidelberg, 2015). doi:10.1007/978-3-662-44395-8_3
165. Nojiri, K. in *Dry Etching Technology for Semiconductors* 11–30 (Springer International Publishing, 2015). doi:10.1007/978-3-319-10295-5_2
166. Ul-Hamid, A. in *A Beginners' Guide to Scanning Electron Microscopy* 77–128 (Springer International Publishing, 2018). doi:10.1007/978-3-319-98482-7_3
167. Encyclopædia Britannica. Scanning electron microscope. *Encyclopædia Britannica* Available at: https://www.britannica.com/technology/scanning-electron-microscope/media/526571/110970. (Accessed: 20th February 2019)
168. Egerton, R. F. in *Physical Principles of Electron Microscopy* 125–153 (Springer US, 2005). doi:10.1007/0-387-26016-1_5
169. Physical Electronics, I. X-Ray Photoelectron Spectroscopy (XPS) Surface Analysis Technique. Available at: https://www.phi.com/surface-analysis-techniques/xps-esca.html. (Accessed: 21st February 2019)
170. Haasch, R. T. in *Practical Materials Characterization* 93–132 (Springer New York, 2014). doi:10.1007/978-1-4614-9281-8_3
171. van der Heide, A. in *X-Ray Photoelectron Spectroscopy* 1–12 (John Wiley & Sons, Inc., 2011). doi:10.1002/9781118162897.ch1
172. Olefjord, I. in *Surface Characterization* **5,** 291–319 (Wiley-VCH Verlag GmbH, 2013).
173. X-ray Photoelectron Spectroscopy (XPS) Reference Pages: Palladium. Available at: http://www.xpsfitting.com/search/label/Palladium. (Accessed: 22nd February 2019)
174. Sauerbrey, G. Verwendung von Schwingquarzen zur Wägung dünner Schichten und zur Mikrowägung. *Zeitschrift für Phys.* **155,** 206–222 (1959).